J. Fluid Mech. (2004), *vol.* 501, *pp.* 71–104.
DOI: 10.1017/S0022112003006967 Printed in the United Kingdom

A model for velocity fluctuations in sedimentation

By PETER J. MUCHA[1], SHANG-YOU TEE[2], DAVID A. WEITZ[2,3], BORIS I. SHRAIMAN[4] AND MICHAEL P. BRENNER[3]

[1]School of Mathematics and Center for Dynamical Systems and Nonlinear Studies,
Georgia Institute of Technology, Atlanta, GA 30332-0160, USA
mucha@math.gatech.edu

[2]Department of Physics, Harvard University, Cambridge, MA 02138, USA

[3]Division of Engineering and Applied Sciences, Harvard University, Cambridge, MA 02138, USA

[4]Department of Physics and Astronomy, Rutgers, The State University of New Jersey,
Piscataway, NJ 08854, USA

(Received 25 March 2002 and in revised form 3 July 2003)

We present a model for velocity fluctuations of dilute sedimenting spheres at low Reynolds number. The central idea is that a vertical stratification causes the fluctuations to decrease below those of an independent uniform distribution of particles, such a stratification naturally occurring from the broadening of the sedimentation front. We use numerical simulations, scaling arguments, structure factor calculations, and experiments to show that there is a critical stratification above which the characteristics of the density and velocity fluctuations change significantly. For thin cells, the broadening of the sediment front (and the resulting stratification) is small, so the velocity fluctuations are predicted by independent-Poisson-distribution estimates. In very thick cells, the stratification is significant, leading to persistent decay of the velocity fluctuations for the duration of the experiment. Estimated stratifications quantitatively agree with the simulations, and indicate the likelihood that previous experimental measurements were also affected by stratification. The velocity fluctuations in sedimentation are therefore not universal but instead depend on both the cell shape and developing stratification.

1. Introduction

A general sedimentation process consists of a collection of heavy particles falling under their own weight through a fluid. In the absence of appreciable inertia, each particle quickly achieves its terminal velocity downward relative to the local fluid velocity – that is, the particles are instantaneously in a state where hydrodynamic drag cancels the external gravitational body force. In general, this is a complicated many-body interaction (see descriptions in, e.g. Mazur & van Saarloos 1982; Brady & Bossis 1988; Ladd 1990). In the slow-settling limit, particle interactions are long ranged: in a spatially infinite system at zero Reynolds number the velocity produced by the motion of a single particle decays like r^{-1}, where r is the distance from the particle. The motion of each particle is therefore influenced by all of the others.

The average rate of settling and its dependence on particle concentration has been throughly studied (e.g. Kermack, M'Kendrick & Ponder 1929; Batchelor 1972;

Davis & Acrivos 1985). However, the long-ranged hydrodynamic interactions cause individual particles to significantly fluctuate about the mean. Despite substantial effort, there is still widespread discord and debate about what sets the size of these fluctuations (e.g. Hinch 1988; Segrè, Herbolzheimer & Chaikin 1997; Brenner 1999; Segrè *et al.* 2001; Ramaswamy 2001, and references therein).

The difficulty in predicting the velocity fluctuations was first brought out by Caflisch & Luke (1985), who demonstrated that a dilute independent distribution of sedimenting particles results in velocity fluctuations $\langle \Delta V^2 \rangle$ that scale linearly with the size L of the container holding the suspension: $\langle \Delta V^2 \rangle \sim V_0^2 \phi L/a$, where V_0 is the terminal Stokes velocity of a particle of radius a, and ϕ is the particulate volume fraction. This result is in stark contrast with most common diffusive processes, in that it implies that the hydrodynamically induced particle diffusivity is not a purely local quantity. Rather, the effective diffusivity here would be determined by a product of ΔV with a correlation length, also set by L in this argument, and would thus increase with the size of the vessel.

Since Caflisch & Luke pointed this out, the velocity fluctuations of dilute sedimenting spheres have been addressed by numerous authors, theoretically (Koch & Shaqfeh 1991; Levine *et al.* 1998), experimentally (Ham & Homsy 1988; Xue *et al.* 1992; Nicolai & Guazzelli 1995; Nicolai *et al.* 1995; Segrè *et al.* 1997; Cowan, Page & Weitz 2000; Guazzelli 2001; Lei, Ackerson & Tong 2001), and numerically (Koch 1994; Ladd 1993, 1996, 1997; Schwarzer *et al.* 1999; Kuusela & Ala-Nissila 2001). Generally speaking, the experimental, theoretical and numerical studies completely disagree with each other. Whereas experiments have generally identified fluctuations that are independent of system size, numerical simulations have typically observed Caflisch & Luke's dependence on system size. It has been argued, however, that simulations are deficient in not tracking sufficiently many particles to capture the proposed saturation (as interpreted from the plot of the Ladd 1996, 1997 simulation data in Segrè *et al.* 1997). A provocative set of recent experiments by Segrè *et al.* (1997) argued that not only are the velocity fluctuations independent of system size, but the correlation length ℓ is universal in terms of the interparticle spacing, $\ell \sim a\phi^{-1/3}$. This modifies the fluctuation scaling to $\langle \Delta V \rangle \sim V_0 \phi^{1/3}$, independent of cell size (Hinch 1988; Segrè *et al.* 1997). Meanwhile, no theoretical mechanism linking the scale of the fluctuations to the interparticle spacing has been clearly identified.

Recent theoretical work has examined the assumptions of the Caflisch & Luke argument, in an effort to uncover the discrepancy between simulations and experiments. Brenner (1999) studied the effect of sidewalls on the hydrodynamics and argued that the fluctuations from a uniform particle distribution between two sidewalls does not differ substantially from the experimental measurements. Luke (2000) studied the effect of stable stratifications of the particle density, and argued that a constant stratification causes the fluctuations to decay continuously in time. Meanwhile, recent numerical simulations by Ladd (2002) demonstrated conditions under which velocity fluctuations could decay below the system-size scaling. However, none of the theoretical or numerical investigations to date has been able to provide a description in quantitative agreement with the experiments.

This paper proposes a model for the velocity fluctuations in sedimentation, which may provide a consistent resolution to this problem. Using a combination of numerical simulations, physical scaling arguments, theoretical calculations, and experimental observations, we argue that the velocity fluctuations in a dilute sedimenting suspension are determined by a combination of two different physical mechanisms. First, number-density fluctuations driven by Poisson statistics create velocity fluctuations on the scale of the small cell dimension. Second, the fluctuations are extremely sensitive to the presence of a tiny vertical stratification. Stratification naturally appears in sedimentation experiments, for multiple reasons: (i) the spreading of the sediment front, driven by the velocity fluctuations themselves and by polydispersity; and (ii) the particle distribution after mixing might contain small stratifications. Even though measurements are typically taken when the sediment front is far from the imaging window, we will demonstrate that for sufficiently large containers, the stratification in the imaging window is enough to change the character of the velocity fluctuations.

The organization of this paper is as follows. In § 2, we calculate the velocity fluctuations for independent, uniform particle distributions, accounting for the hydrodynamic effect of sidewalls. We derive explicit formulae for the spatial dependence of the fluctuations across high-aspect-ratio cells, and we numerically calculate the scaling coefficients for square cells. Section 3 tests these predictions against dilute-limit simulations of up to 4 096 000 particles, developed according to the formulae of Appendix A, demonstrating that the Poisson distribution is dynamically stable in vertically homogeneous systems. The Poisson calculations also accurately predict the spatial dependence of the fluctuations, the scaling of the mean-squared relative displacements, and the temporal fluctuations of the fluctuations (Appendix B). Section 4 compares these results to dilute experiments. The Poisson predictions reproduce most experimental measurements within a factor of two; however, there are serious systematic discrepancies between the Poisson predictions and the experiments, notably a different volume fraction dependence than found by Segrè *et al.* (1997), and also the absence of any time dependence in the predictions of the fluctuations as observed experimentally by Tee *et al.* (2002). Section 5 presents a resolution of these discrepancies in terms of the effects of a particle density stratification. Our simulations indicate that a very small stable vertical stratification changes the velocity fluctuations, in agreement with both a physical argument (§ 5.1) and a theoretical calculation of the structure factor (§ 5.2). We then demonstrate (§ 5.3) that experiments can be affected by such a stratification; in our simulations this stratification arises from the broadening of the sediment front, which increases with the small cell dimension because the initial Poisson-predicted velocity fluctuations increase. Additionally, the critical stratification necessary to change the characteristics of the velocity fluctuations decreases on increasing the small dimension. The model for fluctuations in the presence of stratification, combined with an estimate of the front broadening, indicates that many dilute experiments reported to date may have been affected by stratification. In total, these results suggest a resolution of the apparent disagreements between simulations and experiments measuring the velocity fluctuations.

2. Independent uniform particle distributions

We first consider the simplest prediction for the velocity variance: that where the particles are independently and uniformly distributed. This calculation provides an important benchmark for evaluating the results of simulations and experiments. Consider N identical spherical particles independently Poisson distributed in a $d \times w \times h$ cell with number density $n = N/(dwh)$. The velocity fluctuations at a position $\boldsymbol{r}$ are then given by

$$\langle \Delta V_\alpha^2 \rangle(\boldsymbol{r}) = n \int \mathrm{d}\boldsymbol{r}_0 \, [u_\alpha(\boldsymbol{r}, \boldsymbol{r}_0)]^2, \tag{2.1}$$

where $u_\alpha(\boldsymbol{r}, \boldsymbol{r}_0)$ represents the α-component of the velocity at position $\boldsymbol{r}$ produced by a particle at position $\boldsymbol{r}_0$ (assumed to be mean zero).

Caflisch & Luke (1985) evaluated this integral in the infinite system limit, where $u_\alpha \sim aV_0/|\boldsymbol{r}-\boldsymbol{r}_0|$, so that the integral in (2.1) diverges unless cut off at the system size, L, implying that the fluctuations diverge with this length. However, in a finite cell, the integral converges, and thus provides a quantitative estimate for the size of the velocity fluctuations. In particular, if a screening mechanism exists, as suggested by previous experiments, the velocity fluctuations should be below the value predicted by (2.1).

In a finite cell, the velocity fluctuations are cut off at a scale set by the thinnest dimension of the cell (Brenner 1999). If d is the thinnest dimension of a $d \times w \times h$ cell, then $u_\alpha \sim adV_0/|\boldsymbol{r}-\boldsymbol{r}_0|^2$ for $|\boldsymbol{r}-\boldsymbol{r}_0| \gg d$, so that $\Delta V_\alpha \sim V_0 a\sqrt{nd} \sim V_0\sqrt{\phi d/a}$ for $d \ll w, h$. Breaking the integral in (2.1) into near-field $|\boldsymbol{r}-\boldsymbol{r}_0| \lesssim d$ and far-field $|\boldsymbol{r}-\boldsymbol{r}_0| \gtrsim d$ parts, the near-field contribution scales like

$$\sim n(aV_0)^2 \int_0^d r^2\,\mathrm{d}r\,[1/r]^2 \sim nd(aV_0)^2 \sim V_0^2\phi d/a,$$

while the far field contributes with the same scaling,

$$nd^2(aV_0)^2 \int_d^\infty (rd)\,\mathrm{d}r\,[1/r^2]^2 \sim nd(aV_0)^2 \sim V_0^2\phi d/a.$$

Hence, the velocity fluctuations $\Delta V_\alpha(\boldsymbol{r})$ are given by

$$\Delta V_\alpha(\boldsymbol{r}) = C_\alpha(\boldsymbol{r})\,V_0\sqrt{\phi d/a}. \qquad (2.2)$$

To compare with experiments, we need a quantitative calculation of the prefactor $C_\alpha(\boldsymbol{r})$ of this scaling law, requiring averaging the velocity field produced by particles distributed uniformly in the cell. Here we evaluate $C_\alpha(\boldsymbol{r})$ in the high-aspect-ratio limit, when the depth $d \ll w, h$. This limit applies to many experiments and is computationally the most tractable.

To evaluate this integral, we developed a representation for the velocity field generated by a source particle between two walls, in the point-force limit where that particle is much smaller than distances to the sidewalls. This velocity field was previously calculated by Liron & Mochon (1976); however, their formulae are in the form of slowly converging infinite sums and integrals, and thus could not be efficiently applied to the calculation at hand. Instead, we developed a solution to the alternative problem of no-slip boundary conditions at a pair of parallel sidewalls, with periodic boundary conditions in the other two directions, via a two-dimensional Fourier series expansion. For the dependence perpendicular to the sidewalls (the x-direction) it is necessary to solve a set of ordinary differential equations. Analytical forms for the solutions to these equations are described in Appendix A. In addition, the velocity field incorporated the backflow that each particle produces, by requiring that the mean volume flux of the velocity field across the thinnest cell dimension vanishes (exactly realizing the no-net-flux constraint imposed for calculating the mean velocity by Kermack *et al.* 1929 and Batchelor 1972; indeed, the average velocities in simulations agree with the dilute-limit pair distribution function dependence developed by Batchelor, as applied to these Fourier-truncated point particles).

With this no-slip-sidewalls velocity field we calculate the integral in (2.1) semi-analytically: the contribution from each two-dimensional wavevector is determined in closed form, and the remaining two-dimensional summation is evaluated numerically, truncating the two-dimensional Fourier series with N_k modes in each direction, Richardson extrapolation yielding results in the $N_k \to \infty$ infinite truncation limit. For a uniform particle density, the velocity field statistics are homogeneous in the vertical (z) and the long periodic horizontal (y) directions, but not in the direction perpendicular to the sidewalls (x). The velocity variance thus maintains spatial dependence on this last direction, $\langle \Delta V^2 \rangle(x)$. We find that for x measured from the midplane between the pair of sidewalls, the prefactors are approximated well by quartic polynomials:

$$\left.\begin{aligned} C_x\left(\frac{x}{d}\right) &\doteq 0.275\sqrt{1 - 5.5\left(\frac{x}{d}\right)^2 + 6\left(\frac{x}{d}\right)^4}, \\ C_y\left(\frac{x}{d}\right) &\doteq 0.403\sqrt{1 - 4.7\left(\frac{x}{d}\right)^2 + 2.8\left(\frac{x}{d}\right)^4}, \\ C_z\left(\frac{x}{d}\right) &\doteq 0.865\sqrt{1 - 3\left(\frac{x}{d}\right)^2 - 4\left(\frac{x}{d}\right)^4}. \end{aligned}\right\} \tag{2.3}$$

These formulae apply to high-aspect-ratio cells; other sedimentation experiments have been performed in square $d \times d \times h$ cells, $d < h$ (e.g. Guazzelli 2001). For comparison, we also numerically computed the integral (2.1) for such square cells. (Forced Stokes solutions were calculated on equispaced finite-difference and on pseudospectral Chebyshev grids of varying resolutions and integrated as for (2.1), results varying little for $h \gtrsim 2d$.) At the centre of the cell, we find $C_\alpha \doteq (0.28, 0.28, 0.61)$; additionally, the root-mean-squared fluctuations, averaging the velocity variance over the full cell, are given by the coefficients $C_\alpha \doteq (0.19, 0.19, 0.48)$. The prefactors for the velocity fluctuations in a square cell are thus slightly lower than those in a high-aspect-ratio cell.

We remark that for both square cells and the long horizontal direction in high-aspect-ratio cells, the ratio of the vertical velocity fluctuations to the horizontal fluctuations is approximately 2. In the short horizontal direction of $d \ll w, h$ cells, the velocity fluctuations are approximately $1/3$ of the vertical fluctuations.

3. Simulations of vertically homogeneous sedimentation

The above calculations give quantitative predictions for the velocity fluctuations which hold as long as (a) the dilute assumption applies and (b) the independent uniform distribution is dynamically stable. The principal dilute assumption is that point particles accurately capture the essential interparticle interactions in the low-volume-fraction limit; technically the formulae are asymptotically correct to $O(a/d)$ and $O(\phi)$. Since the ratio $a/d \sim 10^{-2}$ in typical experiments, the dilute assumption is accurate as long as particles remain uniformly distributed on the scale of a few interparticle separations.

To test whether the particles remain independently distributed, we performed simulations of interacting particles in a dilute suspension sedimenting between two parallel no-slip vertical sidewalls separated by a length d, using the velocity fields described in Appendix A. The $d \times w \times h$ computational cells are periodic in the w- and h-directions. Simulations were performed with up to 4 096 000 particles, cell depths d of up to 80 mean interparticle spacings separating the two sidewalls, and Fourier truncations at $N_k \times N_k$ modes with N_k up to 127. The effect of the Fourier truncation is to smooth the spatial extent of the force due to a particle, while maintaining the no-slip conditions on the sidewalls. Our algorithm allows us to carry out simulations over many characteristic times of the particle motion, where single particle motion transitions from ballistic to diffusive behaviour in the long cell directions. Such large calculations are possible because the fluid velocity field, including sidewall effects, is calculated in $O(N_k^2 N \log N)$ operations for N particles and Fourier truncations set by N_k. Details are described in Appendix A.

Requiring resolution of all flows down to the interparticle scale would set $N_k \sim O(N^{1/3})$ and the resulting algorithm then takes $O(N^{5/3} \log N)$ operations. However, since the dominant contributions to the particle velocity fluctuations come from large-scale density fluctuations and fluid motions, one may hope to obtain reasonable agreement with observations by including only a fixed number of N_k modes, set by a desired spatial resolution relative to the cell dimensions, not the interparticle spacing. The long-range nature of the point-force flows yields the Caflisch–Luke scaling, the short-range interparticle detail only influencing the coefficients; indeed, the $C_\alpha(\boldsymbol{r})$ coefficients contain the entire N_k dependence in the Poisson prediction (2.2), (the result quoted in (2.3) coming from the $N_k \to \infty$ limit, as noted there) whereas the effect of the number of particles N appears only in the volume fraction. As visual evidence that even seemingly crude Fourier truncations yield plausible results, figure 1 shows instantaneous particle positions and velocities in a thin slice around the midplane parallel to the walls, for a doubly periodic (in y and z) sidewall (in x) simulation of $N = 256\,000$ particles in a $16d = w = h$ cell, at $N_k = 15$. The upper figure spans the full cell in y and z; the lower figure focuses in on a smaller region, with both dimensions equal to $4d$. In-plane velocities (relative to the downward mean) are indicated by black arrows; velocities perpendicular to the image plane are coloured red (in) to blue (out). Swirls and colour patches are evident, with correlation lengths observably on the scale of the interwall separation, d. Despite the coarse, small-N_k truncation of the hydrodynamic interactions in this simulation, effectively smoothing out the point forces over scales comparable to the thin cell dimension d, the essential long-range properties yield visual details of these swirls that are qualitatively similar to those observed experimentally (as in, e.g. Segrè *et al.* 1997). Again, this is not surprising because the long-range natures of the Fourier truncations and true point forces are the same.

The velocity fluctuations in these simulations are accurately predicted by the Poisson estimate. Figure 2 shows variances of each velocity component versus time from a simulation of $N = 64\,000$ particles initially positioned by random sequential addition with a large exclusion radius. After an initial transient due to the non-independent initial condition, the fluctuations oscillate about constant values which are predicted (the dashed lines) extremely well by the calculations following from (2.1).†

In the units used in figure 2, the time scale $d/\Delta V_z$ is just slightly larger than unity, with the initial transient surviving for a few $d/\Delta V_z$. The relaxation of initial non-Poisson transients to Poisson-predicted velocity fluctuations in similar simulations is consistent with a $d/\Delta V$ time scale. The initially non-independent particle distributions obtained by random sequential addition with exclusion radii are more ordered than Poisson distributions, with smaller density fluctuations and hence smaller initial velocity fluctuations, but the large number of interacting particles statistically randomizes the distribution, generating new density fluctuations and driving the distribution to Poisson on a time scale $\sim d/\Delta V$. This process continues in

---

† We remark that since the simulation velocity fields are truncated at $N_k \times N_k$ Fourier modes, it is also necessary to compare these results with the same truncation for the independent Poisson distribution prediction. This is a technical comment that is an artifact of the way we are doing the numerical calculations, having no bearing on results in the $N_k \to \infty$ limit.

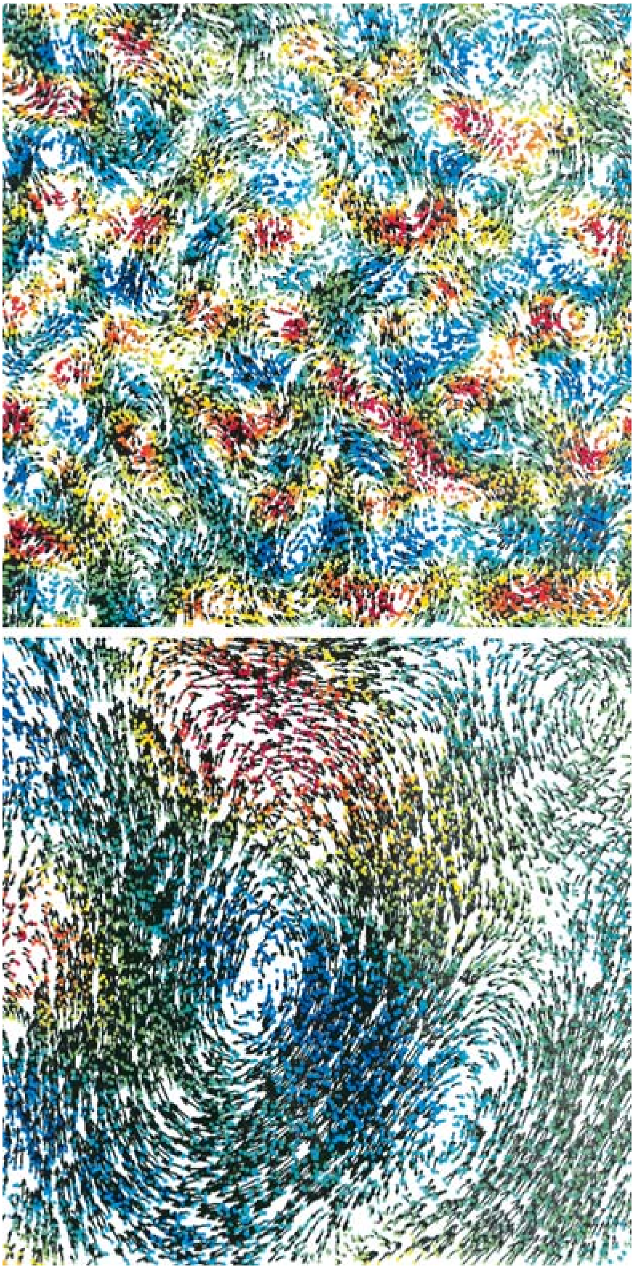

FIGURE 1. Instantaneous particle positions and velocities (relative to the mean) from a simulation of $N = 256\,000$ particles in a $16d = w = h$ cell with sidewalls separated by the short, out-of-plane dimension and periodic ($N_k = 15$) in the other two dimensions. In-plane velocities (relative to the mean) are indicated by arrows. Out-of-plane velocities are colour-coded from red (into) to blue (out of). The top image spans the periodic dimensions, imaging particles near the midplane between the sidewalls; in-plane and out-of-plane velocities both appear to be correlated on the scale of the interplane separation. The bottom image is a close-up of a few swirls, with a wider depth of focus around the midplane.

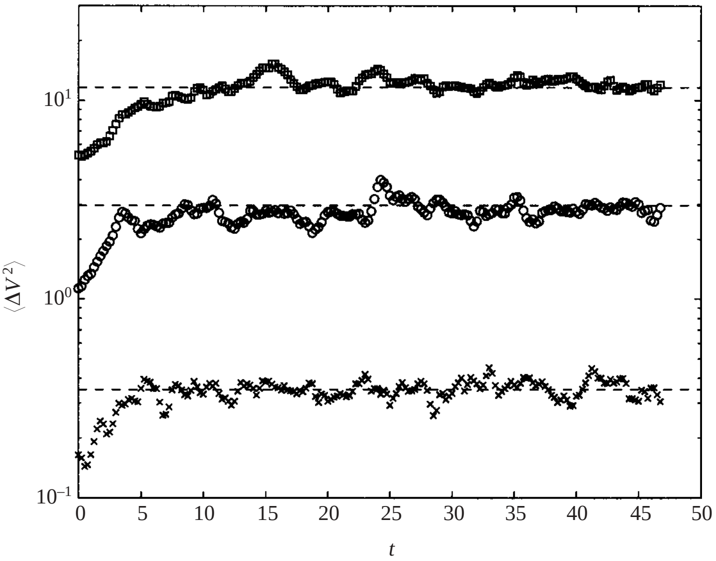

FIGURE 2. Comparison of the Poisson estimates with velocity fluctuations in the x- (×), y- (○), and z- (□) directions observed in an $N = 64\,000$ simulation in a $4 \times 64 \times 64$ side-wall cell at $N_k = 15$, with initial condition generated by random sequential addition with an exclusion radius, i.e. initial particle positions are not initially independent, with smaller density and velocity fluctuations than a Poisson distribution. After an initial transient of time scale $\sim d/\Delta V$, the depth-averaged velocity variances oscillate about a steady-state average that is in good agreement with the independent uniform Poisson position estimates at the same truncation (dashed lines).

the statistically steady Poisson state, where the generation of density fluctuations and their decorrelating destruction occur on the same time scale $\sim d/\Delta V$.

The identification of the Poisson particle distribution as the statistically steady state of the simulations is not limited to the measurement of average velocity fluctuations. A number of other observations from these simulations are accurately captured by the independent Poisson distribution, including (as discussed in Appendix B): (i) spatial dependence of the velocity fluctuations on the interwall coordinate, x; (ii) the scaling of the mean-squared relative particle displacements; and (iii) the higher-order velocity statistics and the size of the temporal fluctuations around the steady-state variance values. Furthermore, attempts to directly measure the particle distributions in simulations in terms of an isotropic pair distribution function indicated relaxation to independent Poisson statistics after the initial transient from an initially non-Poisson distribution.

The cell sizes considered in our doubly periodic-sidewall simulations significantly exceed the conjectured universal length scale of 10–20 mean interparticle spacings, simulations with d up to 80 mean interparticle spacings remaining in agreement with the Poisson estimates, providing no evidence of saturation above the proposed ‘universal’ scale. We have also performed dilute simulations in cells with triply periodic boundary conditions (similar to Koch 1994), with up to $O(10^6)$ particles, with no evidence of deviation from the Caflisch & Luke (1985) scaling. It should be noted that the homogeneity of sedimentation in a triply periodic cell, the pairwise form of the dilute-limit interactions, and the nature of the Stokeslet singularity together ensure the applicability of a theorem due to Pulvirenti (1996) which requires that, in

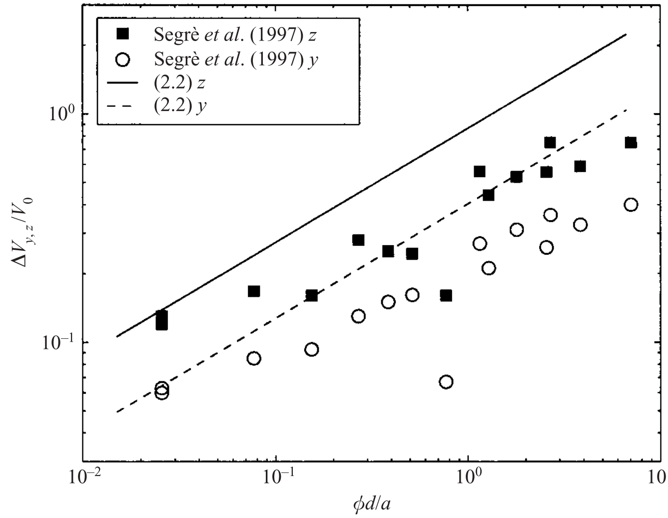

FIGURE 3. Comparison of midplane side-wall Poisson estimate (2.2) with experimental results from figure 3 of Segrè *et al.* (1997). Averaging velocity variances over the middle half of the interplane separation reduces the theoretical estimates (2.3) only mildly, by a factor of 0.95 for ΔV_y, and a factor of 0.967 for ΔV_z.

the $N \rightarrow \infty$ limit, particle positions initially selected from a smooth distribution relax over time to an independent product measure – in this case, an independent Poisson distribution. The horizontal inhomogeneities induced by the presence of sidewalls in our simulations do not appear to change the independent positions outcome of this relaxation process.

4. Comparison with experiments

The above calculations imply that the velocity fluctuations are determined by the small cell dimension and depend on volume fraction through $\Delta V_\alpha = C_\alpha V_0 \sqrt{\phi d/a}$. In contrast, experiments have concluded that velocity fluctuations in large cells are 'universal' with velocity fluctuations that depend on volume fraction through $\Delta V \sim V_0 \phi^{1/3}$. Clearly our results disagree with these conclusions.

Figure 3 shows a comparison between the quantitative predictions (no free parameters) of the Poisson estimate in the midplane between the sidewalls (2.2), (2.3) and the experiments of Segrè *et al.* (1997). Averaging the predictions over the middle half of the cell, as indicated for some of the Segrè *et al.* (1997) data, only decreases the prediction as obtained from (2.3) slightly. The calculations agree with the data quite well at the lowest volume fractions, whereas the measurements deviate from the predictions at higher volume fractions. The discrepancy in ΔV is a factor of 2 at $\phi = 3\%$, and a factor of 3 at $\phi = 5\%$. Similar discrepancies arise when comparing the square-cell Poisson prediction with the measurements of Nicolai & Guazzelli (1995) and Nicolai *et al.* (1995). At the same time, the Poisson predicted ratio $\Delta V_z/\Delta V_y \doteq 2.14$ in the midplane is in good agreement with the measurements (≈ 2, Segrè *et al.* 1997) over the entire range of volume fractions. The predicted ratio $\Delta V_z/\Delta V_y \doteq 3.14$ in the midplane was not measured by Segrè *et al.* (1997), but experiments of Tee *et al.* (2002) show good agreement (≈ 3).

An even more dramatic discrepancy arises in experiments of Tee *et al.* (2002), who demonstrate that for 'thick' enough cells, the velocity fluctuations in a measurement

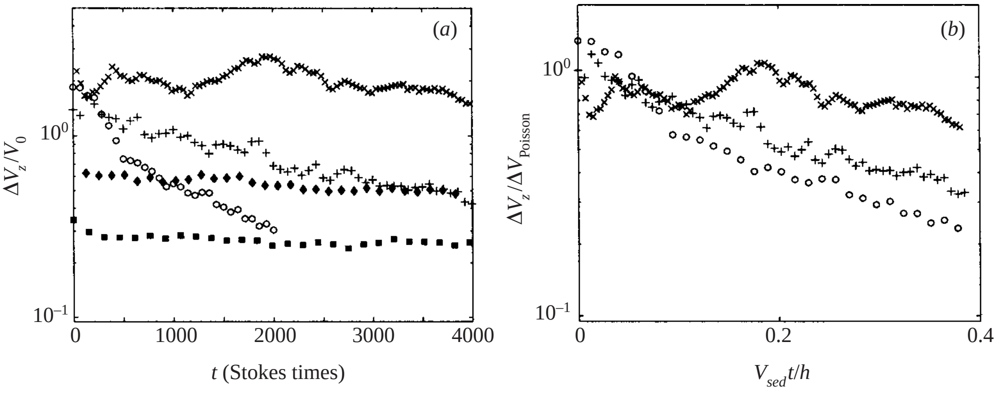

FIGURE 4. Particle image velocimetry (PIV) measurements of ΔV_z in various experiments (see also Tee *et al.* 2002). The sedimenting particles are in a state of low Reynolds number and high Péclet number, and the cell is immersed in a stirred water bath at a temperature of $T = 22.0 \pm 0.1\,^{\circ}\text{C}$. Initial particle distributions are prepared by vigorously shaking the cell, or by stirring with a rotating blade. The measurements are taken in a window of width comparable to d, centred at $z \approx h/3$ from the bottom of the cell. (*a*) $\Delta V_z/V_0$ vs. t in Stokes times; (*b*) decaying ΔV_z relative to the Poisson prediction (2.1) vs. t in sedimentation times h/V_{sed}. Experimental data labelled by volume fraction ϕ and cell dimensions $d/a \times w/a \times h/a$: ◆, 0.4% $189 \times 2830 \times 11\,300$; ○, 1.0% $226 \times 2260 \times 5280$; +, 1.0% $226 \times 2260 \times 10\,600$; ×, 1.0% $755 \times 1890 \times 10\,600$; ■, 0.1% $113 \times 1890 \times 10\,600$. The particle radius is $a = 26.5 \pm 1.8\,\mu\text{m}$.

window do not reach steady state, but decay over the entire time of the experiments. By contrast, fluctuations in 'thin' cells appear to decay to a constant value after an initial transient. These behaviours are shown in figure 4 (see also Tee *et al.* 2002).

Under no circumstances do the vertically homogeneous simulations described above yield such persistent decay of the fluctuations. The transient visible in figure 2 when the particle distribution adjusts from a non-independent initial distribution to an independent distribution occurs on a short time scale and does not persist after the Poisson distribution is obtained. These discrepancies are substantial enough to suggest that there is another effect in the experiments that goes beyond the physics heretofore included in the simulations. We thus considered a number of additional effects, including:

(*a*) Corrections to the particle velocity, including higher-order hydrodynamic corrections, as well as the dependence of the particle mobility on the distance to the wall, due to wall drag. Neither of these had an appreciable effect on the fluctuations.

(*b*) Shearing the walls of the system and introducing arbitrary $v_z(x)$ flows to the particle motion, in an attempt to influence the mixing properties of the suspension. Neither had any effect on the velocity fluctuations around the resulting averages.

(*c*) Including the effect of finite polydispersity of the particle distributions. For the magnitude of polydispersity that exists in the experiments this does not affect the velocity fluctuations in vertically periodic simulations, other than the quantitatively predictable increase in the variance due to the range of particle falling velocities.

(*d*) The hydrodynamic effect of the bottom of the cell. Since the particles in the imaging window are far from the bottom in units of the cell depth this is not important, the contribution to the variance of the hydrodynamics decaying quickly beyond the distance of the cell depth, d.

(*e*) The effect of small cell tilt, i.e. the Boycott (1920) effect. Although the Boycott effect significantly influences the velocity fields and fluctuations for cell tilts of more than a few degrees, as observed upon appropriately modifying our simulations, the experiments are below this limit. We tested for the Boycott effect experimentally by measuring the velocity fluctuations as a function of small tilt angles and there is no significant effect for tilt angles of order a degree.

(f) The effect of temperature gradients across the sample cell. A very small temperature gradient across the cell depth (a few mK) can cause buoyancy fluctuations which compete with the velocity fluctuations, since the buoyancy forces from temperature gradients across a region of the cell scale like the volume of the region, whereas the velocity fluctuations scale like the square root of the volume. However, most experiments for velocity fluctuations are performed in stirred tanks, with temperature differences that are unlikely to be important.

The crucial observation to explain the discrepancy was suggested to us by the initial velocity fluctuations. When $\Delta V_{\mathrm{initial}} \lesssim V_0$ the fluctuations remain in steady state, whereas persistent decay occurs typically when $\Delta V_{\mathrm{initial}} \gtrsim V_0$. We compare the importance of V_0 as an independent physical parameter here with the pairwise dilute point-force interactions, e.g. as in (4.1) below, wherein V_0 appears in the product $f/\eta \sim aV_0$ and as a constant shift $-V_0\hat{z}$. In a vertically homogeneous environment, however, such as with vertically periodic boundary conditions or far from boundaries in a purportedly homogeneous bulk, the constant contribution is trivially removed by a Galilean shift, implying that V_0 should then only appear in the product aV_0. The observation that the single particle sedimentation velocity V_0 enters into the problem independently here thus indicates that the vertical homogeneity has been broken and is affecting the dynamics.

We therefore carried out a set of vertically inhomogeneous simulations for various initial values of $\Delta V/V_0$. To break the vertical symmetry we added top and bottom surfaces to the cell. As argued above, the hydrodynamic effects of these surfaces are relatively unimportant, decaying rapidly on distances larger than d; their lowest-order hydrodynamic effects can be captured simply by images (Blake 1971). Their more important roles here are as impenetrable barriers restricting particle motion, building up the particle population at the bottom and allowing the sediment front to broaden as it falls. The simulations compute the velocity of each particle as

$$\frac{\mathrm{d}\boldsymbol{r}_i}{\mathrm{d}t} = -V_0\hat{z} + \sum_{j\neq i} \frac{f}{\eta}\boldsymbol{U}(\boldsymbol{r}_i, \boldsymbol{r}_j), \tag{4.1}$$

where f is the magnitude of the external force on a particle, η the fluid viscosity and $\boldsymbol{U}(\boldsymbol{r}_i, \boldsymbol{r}_j)$ is the velocity produced at $\boldsymbol{r}_i$ by a unit downward force located at $\boldsymbol{r}_j$ ($\boldsymbol{U} = -\boldsymbol{S}$, determined in Appendix A). In terms of the force f, the Poisson prediction for the velocity fluctuations (Caflisch & Luke 1985) scales like $\Delta V \sim (f/\eta)\sqrt{nd}$. One can therefore increase ΔV relative to V_0 by increasing the number density of particles n, increasing the cell depth d, or increasing f/η relative to the settling velocity V_0, the latter being fixed physically by the Stokes drag law. In the simulations, however, this relationship need not be obeyed, and we can thereby artificially explore high $\Delta V/V_0$ by increasing f relative to V_0 (alternatively thought of as increasing the effective radius a, since the particles are points). This device preserves the physics of hydrodynamically interacting particles while allowing simulation of a wider range of $\Delta V/V_0$ than would otherwise be possible without considering prohibitively large numbers of particles.

Figure 5 shows velocity fluctuations from three different simulations as a function of time for three different initial $\Delta V_z/V_0 \approx 0.1$, 1, and 10. For the smallest fluctuations,

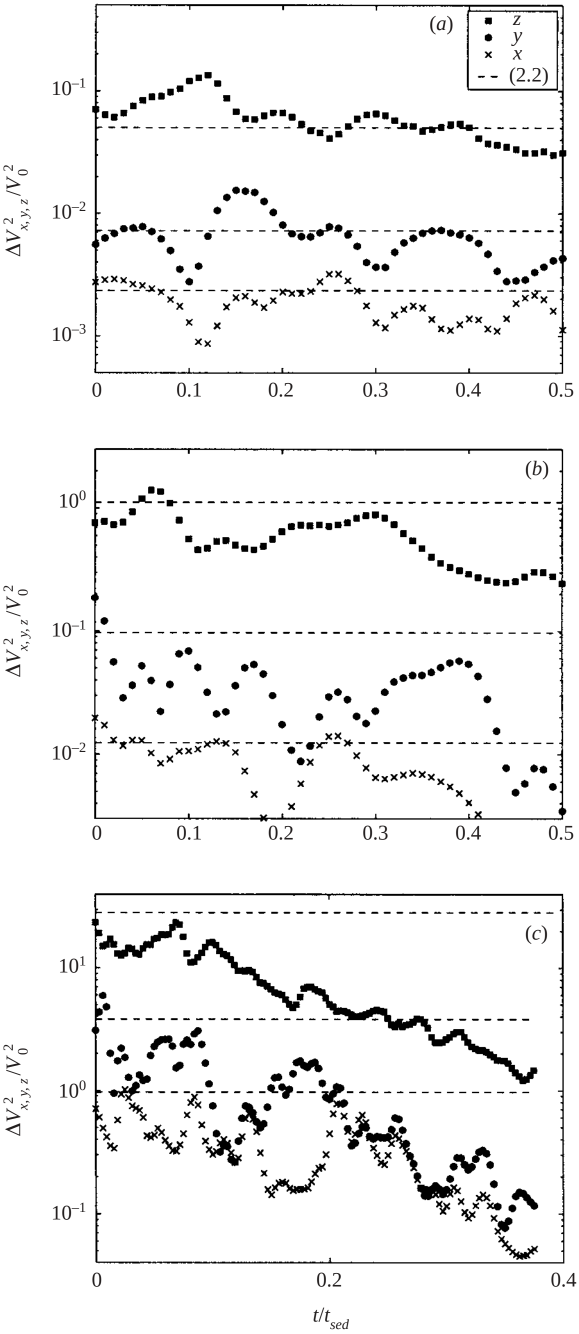

FIGURE 5. Velocity variances in each direction in three different simulations, measured in windows $\approx h/3$ above an imposed impenetrable cell bottom, showing deviation from the homogeneous Poisson estimates (dashed lines) as the initial fluctuations, well-predicted by the Poisson estimates, are increased. Indicated times are in units of the total sedimentation time, $t_{\text{sed}} = h/V_{\text{sed}}$. The data in (*a*) are from an $N = 10\,000$ simulation in a $100 \times 300 \times 1000$ cell with the measurement window $0.3 < z/h < 0.35$; for (*b*), $N = 100\,000$ in a $50 \times 150 \times 600$ cell with measurement window $0.25 < z/h < 0.333$; and for (*c*), $N = 50\,000$ in a $10 \times 30 \times 80$ cell with measurement window $0.3 < z/h < 0.375$. The centre of the front remains far from the measurement windows at the times plotted.

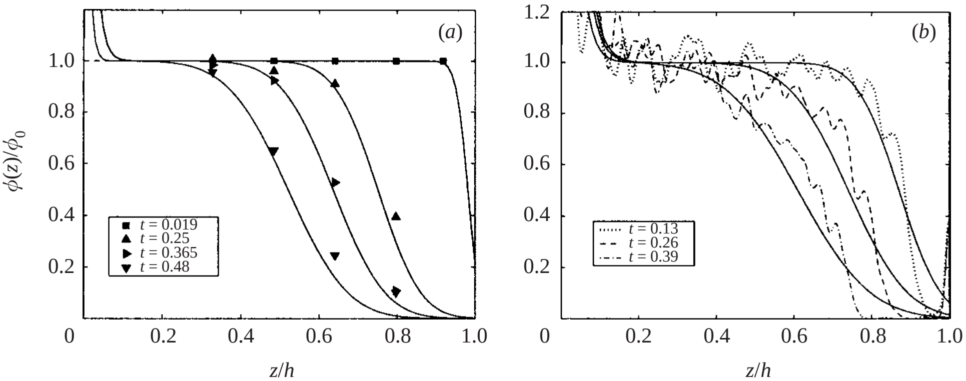

FIGURE 6. Concentration profiles $\phi(z)$ for height z above the bottom of the cell at different times, compared with results from one-dimensional constant-diffusivity advection–diffusion estimates (solid lines): (a) PIV experiment at $\phi_0 = 1\%$ in a $113a \times 1130a \times 4830a$ cell (see also Tee *et al.* 2002), and (b) dilute-limit simulation of $N = 10\,000$ particles in a $10 \times 30 \times 100$ cell with Fourier truncation $N_k = 31$. Times are in units of the total sedimentation time, h/V_{sed}.

the velocity fluctuations appear constant in time, and quantitatively agree with the predictions of the independent Poisson distribution. For the middle case of figure 5, where $\Delta V_z/V_0 \sim 1$, the observed fluctuations dip significantly below the Poisson prediction, where they appear to remain roughly constant until the sediment front gets close to the imaging window. For the largest $\Delta V/V_0$, the velocity fluctuations decay throughout the simulations. The trends and magnitudes of the effects in these simulations agree with those of the experiments. These vertically inhomogeneous simulations therefore seem to contain the necessary interactions to understand all of the features of the velocity fluctuations in dilute sedimentation.

5. Stratification

The key physical difference giving these three different regimes for the velocity fluctuations is the extent of a vertical stratification of the particle concentration in the measurement window. This is demonstrated in figure 6, where we plot the particle concentration as a function of vertical distance from the bottom of relatively thick cells from an experiment (figure 6a) and a simulation (figure 6b). The spreading is more severe in thick cells than in thin ones. This is because the initial hydrodynamic diffusivity $D \sim \Delta V_{\mathrm{init}} L$ increases with increasing cell thickness. When $\Delta V > V_0$, the velocity fluctuations cause the front to spread faster than it falls. Thus, a significant stratification can exist when the front itself is far from the imaging window, that is, while concentrations in the measurement window remain close to the initial concentration.

That stratification can affect velocity fluctuations was demonstrated by Luke (2000). Luke argued that velocity fluctuations continually decrease in a medium with a constant stratification, imposed by some unknown external means. Although we agree with Luke's description of the physical mechanism causing the fluctuations to decay, we disagree with his conclusion that a constant stratification produces continually decaying fluctuations. Rather, we argue below that a constant stratification leads to statistically steady velocity fluctuations at long times which can be smaller than those predicted by the Poisson estimate. Persistent decay of the velocity fluctuations may then occur in experiments (Tee *et al.* 2002) and in simulations under conditions where the local stratification (in a measurement window seemingly far from the front) continually increases with time.

We first present physical arguments for this point of view (similar to those presented in Tee *et al.* 2002) and then present a stochastic model for the fluctuations leading to a structure factor calculation. Neither the scaling from physical arguments nor the model structure factor are rigorously obtained, but the results are shown to agree quantitatively with simulations and experiments. Finally, we describe the consequences of these arguments for interpreting sedimentation experiments.

5.1. *Physical argument*

Velocity fluctuations are driven by fluctuations in particle number, as described by Poisson statistics in a vertically homogeneous random sample. A region of size ℓ has a typical concentration fluctuation of $\Delta\phi \approx \sqrt{\phi a^3/\ell^3}$; its velocity is determined by balancing its buoyant weight, $\Delta\phi\ell^3\Delta\rho g \sim \Delta\phi\ell^3(\eta V_0/a^2)$, with its Stokes drag, $\sim \eta\ell\Delta V$, giving $\Delta V_\ell = C V_0\sqrt{\phi\ell/a}$ (Hinch 1988). The dominant ΔV in a homogeneous sediment is then set by the smallest cell dimension $\Delta V = C V_0\sqrt{\phi d/a}$, because the above arguments are cut off at lengths $\ell > d$. The velocity fluctuations lead to long-time diffusive mean-squared displacements and an effective diffusivity, $D \sim \ell\Delta V$. If this effective diffusion is the dominant process acting on the density fluctuations on a given length scale, the production and destruction of fluctuations due to randomness is then on the same time scale, $\tau_D \sim \ell^2/D \sim \ell/\Delta V$, advecting a distance $\sim \ell$ in their lifetime. This balance between production and destruction of fluctuations due to randomness drives the vertically homogeneous system to an independent Poisson particle distribution (as in, e.g. the simulation results in figure 2).

Even a very small stratification can substantially modify the above argument. If the change in concentration due to stratification is greater than the $\Delta\phi$ concentration fluctuations, the buoyancy mismatch is lost, and the fluctuation at such length scales can no longer advect as far. For a locally linear decrease in ϕ with height, $\phi = \phi_0(1-\beta z)$ $(\beta > 0)$, the stratification causes the lifetime of a fluctuation's motion to be limited to $\tau_S \sim H/\Delta V$, where $H \sim \Delta\phi/(\beta\phi_0)$ is the length scale over which stratification changes ϕ by $\Delta\phi$. The loss of the buoyancy mismatch for $\ell \gtrsim H$ thus sets $\tau_S \lesssim \tau_D$. We speculate that density fluctuations at such large scales are being suppressed faster (on the time scale τ_S) than they are generated by randomness (on the diffusive time scale τ_D). The largest remaining fluctuations are thus on the scale $\ell \sim H \sim \sqrt{\phi_0 a^3/\ell^3}/(\beta\phi_0)$, giving

$$\ell \sim a\phi_0^{-1/5}(\beta a)^{-2/5}, \tag{5.1}$$

with velocity fluctuations

$$\Delta V \sim V_0\phi_0^{2/5}(\beta a)^{-1/5}. \tag{5.2}$$

These arguments for stratification control of the fluctuations apply only when the size of the cut off fluctuations are smaller than the cell depth $\ell < d$; larger fluctuations are controlled by the small cell dimension, d. Setting $\ell \sim d$ yields the critical stratification:

$$\beta_{\text{crit}} \sim a^{3/2}d^{-5/2}\phi_0^{-1/2} = (d\sqrt{N_d})^{-1}, \tag{5.3}$$

where N_d is the number of particles in a volume of radius d. This critical stratification decreases rapidly as the cell thickness increases. For the Tee *et al.* (2002) experiments, $10^{-4} \lesssim N_d^{-1/2} \lesssim 10^{-2}$, stratifications significantly smaller than 1% across a vertical distance of order d typically being sufficient to suppress the independent Poisson velocity fluctuations.

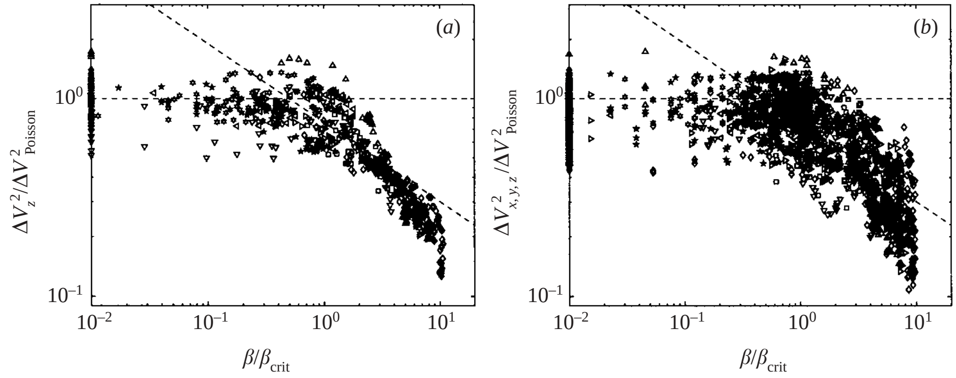

FIGURE 7. Instantaneous velocity fluctuations ((*a*) ΔV_z^2 and (*b*) $\Delta V^2_{x,y,z}$), relative to the Poisson prediction (2.2), versus measured stratification of the smoothed particle concentration, from a series of $N=50\,000$ particle, $N_k=31$ simulations in $8d=w=h$ cells at eight different hydrodynamic interaction strengths. Measurements are taken from a window height $z\approx h/3$ above the bottom of the cell. Negative β (dynamically unstable) and $\beta<10^{-2}\beta_{\mathrm{crit}}$ data ($\beta_{\mathrm{crit}}\equiv[\phi d^5/a^3]^{-1/2}$) are collected on the left-hand edges of the plots. At small stratifications, the velocity variances fluctuate about the Poisson prediction. At large stratifications, the fluctuations appear to be $\Delta V^2/\Delta V^2_{\mathrm{Poisson}}\approx(2\beta/\beta_{\mathrm{crit}})^{-2/5}$ (decaying dashed lines), in agreement with the stratification scaling (5.2), with slight downward bias at very large stratifications where the correlation length is of the same scale as the spatial resolution of the Fourier truncation.

Figure 7 presents simulations comparing instantaneous velocity fluctuations in a measurement window with simultaneous measurements of the local vertical stratification of the number density (smoothed on scales comparable to the cell depth), taken from multiple simulations spanning each of the qualitative behaviours of the velocity fluctuations. No time averaging of the data has been performed. Almost all of the data in the figure are taken when the window is still far from the front, with local volume fractions $\phi>0.95\phi_0$ close to the initial concentration ϕ_0, except a small number of the largest β values that are included, where ϕ is as small as $\approx 0.9\phi_0$. Meanwhile, the observed velocity variances (proportional to ϕ in the Poisson prediction) are suppressed by a factor as large as ≈ 4. The figure clearly demonstrates that when the stratification β is smaller than $\approx\frac{1}{2}\beta_{\mathrm{crit}}=\frac{1}{2}(d\sqrt{N_d})^{-1}$ the velocity fluctuations quantitatively agree with the vertically homogeneous predictions of § 2; when $\beta\gtrsim\frac{1}{2}\beta_{\mathrm{crit}}$ the velocity fluctuations decrease below the Poisson value in a manner consistent with (5.2).

The stratification in these monodisperse simulations originates from diffusive spreading of the sediment front; when $\Delta V/V_0$ is small, this diffusive spreading creates a vertical stratification that remains small compared to β_{crit} far from the front, and therefore the correlation length and the resulting velocity fluctuations are controlled by the smallest cell dimension, d. On the other hand, for large initial ΔV, there is significant diffusion of the front, so the stratification $\beta>\beta_{\mathrm{crit}}$ in the measurement window. This stratification (and hence ΔV) is time dependent, owing to the continual spreading of the front.

That such stratifications might be present in measurement windows seemingly far from the front is illustrated by examining individual simulations. The velocity fluctuations from single simulations of $N=400\,000$ particles and $N=50\,000$ particles are plotted in figure 8 along with the concentration profiles averaged over identified time intervals. The initial condition here is of independently positioned particles filling

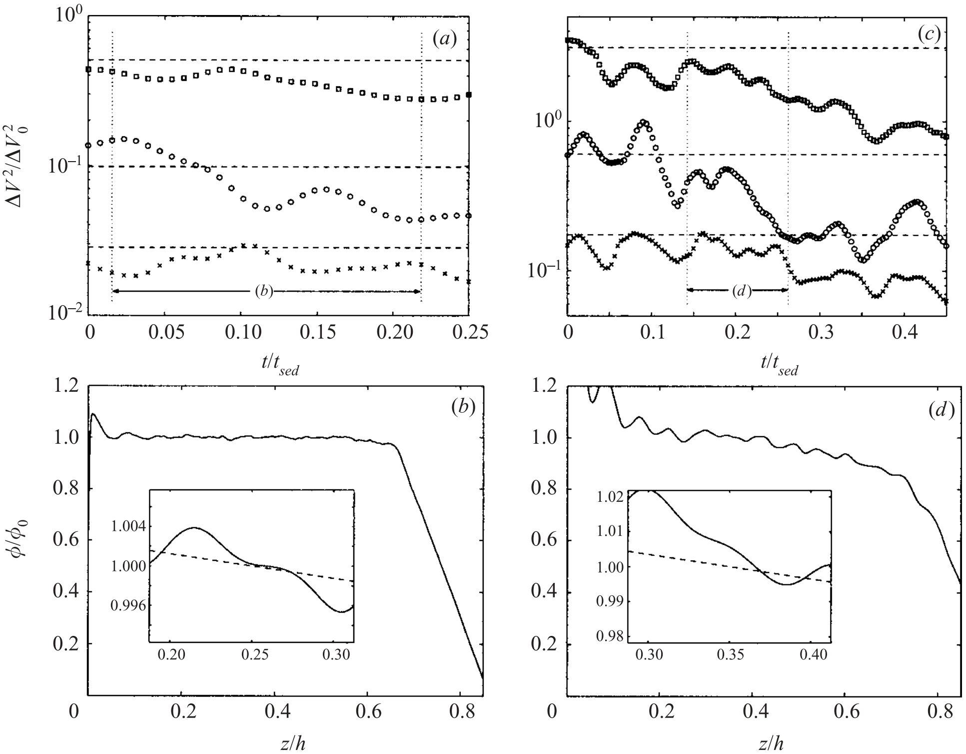

FIGURE 8. Velocity fluctuations and concentration profiles from a pair of simulations in $8d = w = h$ cells with Fourier truncation $N_k = 31$: (*a*) velocity fluctuations of $N = 400\,000$ particles, relative to the Poisson prediction (horizontal dashed lines), measured in a window $0.2 < z/h < 0.3$, over times reported in terms of $t_{\text{sed}} = h/V_0$, and (*b*) the smoothed concentration profile, time-averaged over the interval indicated by the vertical dashed lines in (*a*); (*c*) velocity fluctuations of $N = 50\,000$ particles for larger hydrodynamic forcing, measured in a window $0.3 < z/h < 0.4$, and (*d*) time-averaged concentration profile over the indicated interval. The dashed line in the insets of (*b*) and (*d*) indicates the crossover stratification $\frac{1}{2}\beta_{\text{crit}}$ between fluctuations determined by cell size and those set by the stratification. These observed time-averaged stratifications in the measurement windows are thus of the order necessary (e.g. figure 7) to suppress velocity fluctuations by the observed factor below the Poisson prediction according to the model scaling. The insets, centred in the measurement windows, are over heights $= d$, slightly larger than the measurement windows.

the lower 7/8 of the cell. The concentration profiles plotted in figures 8(*b*) and 8(*d*) include time averaging over the intervals indicated in figures 8(*a*) and 8(*c*), respectively, each being $\approx d/\Delta V_z$ in order to describe the average concentration profile present over the lifetime of the largest swirls. Because of this time averaging, the concentration profile indicated in the front itself is significantly broader in these figures than is actually present. Meanwhile, the measurement windows for these velocity fluctuations would apparently be far from both the container bottom and the cell front, while the net stratification across the measurement window in both cases is clearly in excess of the $\frac{1}{2}\beta_{\text{crit}}$ stratification sufficient to suppress velocity fluctuations. For comparison, the observed suppressions of the velocity variances to $\approx 80\%$ and $\approx 60\%$ of the Poisson predictions is indicated in the scalings and figure 7 by stratifications $\beta \approx 0.9\beta_{\text{crit}}$ and $\beta \approx 1.8\beta_{\text{crit}}$, respectively, of the same magnitude as the observed stratifications in the insets of figure 8(*b*, *d*).

We remark that there are other causes for stratification in experiments, the most important of which are (*a*) polydispersity of the particle sizes, causing additional spreading of the sediment front over that caused by the velocity fluctuations themselves; and (*b*) the initial distribution of particles is not perfectly mixed, and could contain an initial stratification. The latter is hard to quantify in general, but it seems likely to be important. Indeed, we have observed significant variation in the fine details of the decaying fluctuations with time at the same physical parameters from one run to the next, both in the experiments and simulations, while the gross behaviour of persistent decay far from the front in thick cells remains robust.

It is important to remark that in general the effect of stratification is pronounced in thick cells for two different reasons: first, the critical stratification decreases rapidly with cell thickness; second, the velocity fluctuations are enhanced in thick cells leading to enhanced spreading of the front (and thus producing larger stratifications).

5.2. *Stochastic continuum model*

The above arguments can be developed more quantitatively by studying a continuum model of the sedimentation dynamics of equation (4.1). Instead of tracking the locations of each of the individual particles, we describe the sediment with a particle volume fraction $\phi(\boldsymbol{r},t)$ and particle velocity $\boldsymbol{u}(\boldsymbol{r},t)$ (relative to V_{sed}). Both ϕ and $\boldsymbol{u}$ are taken here to be smooth, averaged quantities that ignore the microscopic details of individual particle motions. Their time evolution is governed by conservation of mass and the stress balance in the fluid phase:

$$\partial_t\phi + \nabla\cdot[\boldsymbol{u}(\boldsymbol{r},t)\phi - \boldsymbol{D}\cdot\nabla\phi + \boldsymbol{\xi}(\boldsymbol{r},t)] = 0, \tag{5.4}$$

$$\nabla p = \eta\nabla^2\boldsymbol{u} - \tfrac{9}{2}\hat{\boldsymbol{z}}\eta V_0\phi/a^2, \qquad \nabla\cdot\boldsymbol{u} = 0. \tag{5.5}$$

Here both $\boldsymbol{D}\cdot\nabla\phi$ and $\boldsymbol{\xi}$ represent discreteness effects, quantifying the difference between the dynamical equation for the particle motions and this continuum model. The $\boldsymbol{D}\cdot\nabla\phi$ term represents long-time long-wavelength deviations between the direct advection of averaged quantities and the microscopic dynamics of (4.1), explicitly ensuring large-scale diffusive motion at time scales longer than the swirl turnover time. That is, this diffusive term is appropriate for concentration variations over length scales that are large compared with the correlation length and time scales that are large compared with the turnover time. Importantly, this is where the velocity fluctuations enter into the model, with $D\sim\ell\Delta V$, in agreement with the observation of effectively diffusive particle transport on large scales due to the fluctuations. The additional particle flux $\boldsymbol{\xi}$ represents short-wavelength degrees of freedom in the particle dynamics that are otherwise not accounted for because of the averaging inherent in both ϕ and $\boldsymbol{u}$ in this continuum model.

For simplicity, we model $\boldsymbol{\xi}$ as uncorrelated white noise, so that $\langle\xi_\alpha(\boldsymbol{r},t)\xi_\gamma(\boldsymbol{r}',t')\rangle = v_p\phi\mathcal{N}_{\alpha\gamma}\delta(\boldsymbol{r}-\boldsymbol{r}')\delta(t-t')$, with $v_p=(4\pi/3)a^3$ and $\mathcal{N}$ characterizing the strength of the noise. The stochasticity of this variable in the model represents the continuous state of unknowns in the numerous microscopic degrees of freedom that have been otherwise averaged out. In what follows, we will demonstrate that this continuum model, with white noise and diffusion included explicitly, provides a consistent and semi-quantitative description of our simulations and the experiments. The reader should note, however, that the inclusion of a noise source to model the deterministic microscopic details in sedimentation is currently the subject of controversy. For example, E. J. Hinch (private communication) believes that a continuous noise source model is inappropriate because the physical noise source is in the initial conditions. For added simplicity, we also treat both the particle diffusivity D and the noise strength $\mathcal{N}$ as isotropic. A similar continuum description, including anisotropy in D and $\mathcal{N}$, was previously employed by Levine *et al.* (1998) in an attempt to describe renormalized screening mechanisms.

In a uniform system, the advection velocity in (5.4) is irrelevant at leading order in $(\phi - \phi_0)$ density fluctuations because of the homogeneity of the particle concentration ϕ_0. A straightforward calculation then gives the steady-state structure factor, assuming homogeneity away from external boundaries, as (e.g. Levine *et al.* 1998)

$$S(q) = \frac{1}{v_p \phi} \int \mathrm{d}\boldsymbol{r} \, \langle \phi(\boldsymbol{r}) \phi(0) \rangle \mathrm{e}^{-\mathrm{i}\boldsymbol{q}\cdot\boldsymbol{r}} \sim \frac{\mathcal{N}}{D}. \tag{5.6}$$

By (5.5), the velocity variance $\Delta V^2 = \langle u^2 \rangle$ is then given by

$$\langle \Delta V^2 \rangle \sim n \int \mathrm{d}\boldsymbol{q} S(\boldsymbol{q}) \left[\frac{aV_0}{q^2 + d^{-2}} \right]^2, \tag{5.7}$$

where d is the thin cell dimension, the denominator $q^2 + d^{-2}$ being used here to cut off the $1/r$ flows beyond that length, the precise form of this cut off being unimportant in the scalings considered below. Substituting (5.6) into (5.7) gives the velocity variance scaling like $\langle \Delta V^2 \rangle \sim (aV_0)^2 nd\mathcal{N}/D$. This is precisely the Caflisch & Luke (1985) scaling in the small cell dimension, in agreement with the calculations of § 2, provided that $\mathcal{N}/D \sim 1$, i.e. the noise coefficient is proportional to the diffusivity.

Modifying this calculation to include stratification, we linearize (5.4) about a locally linear stably stratified base state, which we will find sufficient to indicate suppression of fluctuations. We write $\phi = \phi_0(1 - \beta z) + \varphi$, $\beta \geqslant 0$, where φ are the fluctuations, assumed to be much smaller than ϕ_0. Again, we assume that this locally linear stratification persists over a length scale longer than the correlation length ℓ and over a time scale longer than the swirl turnover time $\ell/\Delta V$. Unstable stratifications, $\beta < 0$, are not considered here. To leading order in φ the dynamics are then governed by

$$\partial_t \varphi - \tilde{u}_z \beta \phi_0 = D\nabla^2 \varphi + \nabla \cdot \boldsymbol{\xi}, \tag{5.8}$$

$$\nabla p = \eta \nabla^2 \tilde{\boldsymbol{u}} - \tfrac{9}{2} \hat{\boldsymbol{z}} \eta V_0 \varphi / a^2, \qquad \nabla \cdot \tilde{\boldsymbol{u}} = 0, \tag{5.9}$$

for D constant or varying slowly in space. Because anisotropies in the noise and diffusivity have been ignored, the above dynamics lead to an isotropic structure factor in steady state, given by

$$S(q) \sim \frac{\mathcal{N} q^2}{Dq^2 + A\beta V_0 \phi_0 / [a^2(q^2 + d^{-2})]}, \tag{5.10}$$

where $A > 0$ is a dimensionless constant. The velocity fluctuations are then

$$\langle \Delta V^2 \rangle \sim n \int \mathrm{d}\boldsymbol{q} \, \frac{\mathcal{N} q^2}{Dq^2 + A\beta V_0 \phi_0 / [a^2(q^2 + d^{-2})]} \left[\frac{aV_0}{q^2 + d^{-2}} \right]^2. \tag{5.11}$$

Equation (5.10) indicates that at sufficiently small q (long wavelengths), the denominator of $S(q)$ increases relative to the numerator, so that $S(q)$ decreases below unity, implying that long-range density fluctuations have been suppressed. This describes the physical process of long-wavelength fluctuations decaying away faster than they are generated in the presence of such stratification.

At sufficiently small stratifications, the β term in the $S(q)$ denominator is negligible compared to Dq^2 over the $\boldsymbol{q}$ values contributing to the (5.11) integral, $|\boldsymbol{q}| \gtrsim d^{-1}$, and the Caflisch & Luke scaling is reobtained. At large stratifications, (5.11) gives the same scalings for velocity fluctuations and correlation length as in § 5.1, provided that the stratification is large enough so that $\ell = (q^*)^{-1}$, given by $D(q^*)^2 \sim \beta V_0 \phi_0 / [a^2 (q^*)^2]$, is small relative to the cell depth d. The length ℓ then cuts off the integral in (5.11), instead of d, giving

$$\langle \Delta V^2 \rangle \sim (a V_0)^2 n (q^*)^{-1} \mathscr{N} / D \sim V_0^2 \phi / (a q^*) \sim V_0^2 \phi_0 \left[\frac{D}{a^2 \beta V_0 \phi_0} \right]^{1/4}, \qquad (5.12)$$

where we have again used $\mathscr{N}/D \sim 1$. Both the velocity fluctuations and the correlation length are then in terms of the unknown diffusivity. However, we take $D \sim \ell \Delta V$ since the velocity fluctuations determine the hydrodynamically induced diffusivity. This relation, combined with the above relations for ΔV and $\ell = (q^*)^{-1}$ yields

$$D \sim a V_0 \phi_0^{1/5} (\beta a)^{-3/5}, \qquad (5.13)$$

which in turn gives $\ell = (q^*)^{-1} \sim a \phi^{-1/5} (\beta a)^{-2/5}$ and $\Delta V \sim V_0 \phi^{2/5} (\beta a)^{-1/5}$, exactly as found above in equations (5.1) and (5.2).

Again, the above derivation assumes that $q^* \gg d^{-1}$. If $q^* \ll d^{-1}$, then the formula (5.11) implies that the fluctuations are given by the uniform Poisson distribution, as we have found. This simple isotropic $S(q)$ model thus contains both regimes covered by the physical arguments in § 5.1. Intermediate between these two regimes, both stratification and wall effects become important on the same scale, each term contributing in the $S(q)$ form (5.10). While a number of the above steps may be reasonably regarded as uncontrolled approximations (ignoring anisotropic effects, the time evolution to the steady-state structure factor, and non-white statistics of $\boldsymbol{\xi}$), this $S(q)$ model will be found to be in good agreement with the simulations and previous experimental measurements, as detailed in § 5.3.2 below.

5.3. *Comparison with experiments*

Finally, we compare the results above to concentration profiles, occupancy statistics, and velocity fluctuations measured in experiments.

5.3.1. *Spreading of the sediment front*

An important component of our argument is the fact that the spreading of the sediment front produces a stratification in our simulations. It is therefore useful to estimate this effect in experiments. To this end, here we use a crude model to estimate the spreading of the sediment front for $\phi = \phi(z, t)$ only varying in the vertical ($\hat{z}$) direction, with

$$\partial_t \phi - V_0 \partial_z \phi = D \partial_{zz} \phi, \qquad (5.14)$$

assuming that the sediment is very dilute (ignoring hindered settling effects) and taking D to be constant for simplicity (ignoring spatial and temporal dependence of the diffusion coefficient due to suppressed velocity fluctuations at different stratifications, which becomes especially incorrect in the immediate vicinity of the front itself), with ΔV set by Poisson statistics and $D = K \ell \Delta V$, where K is an $O(1)$ constant (values of which can be determined from the simulations).

Experimental measurements of particle concentration as a function of both time and position are obtained by monitoring the attenuation of the total transmitted light in a particle image velocimetry (PIV) experiment, and using Beer's law to determine ϕ. Initially, ϕ is relatively constant along the cell height; however the profile quickly stratifies. As shown by the solid lines through the data in figure 6 solutions to (5.14) with constant diffusivity D fit the immediate vicinity of the sediment front poorly, as expected. However, despite the crude approximation, including the complete neglect of polydispersity in the experiments, the constant-D solutions are remarkably near measurements taken further from the front, both in our PIV experiments (figure 6*a*) and in our dilute-limit simulations (figure 6*b*). Thus, the model equation (5.14) can be used to quantitatively estimate the magnitude of the possible stratification far from the front.

Since we will subsequently use this simple diffusion model to estimate stratifications larger than critical stratification in previous experiments, it is worth summarizing the major errors in the model:

(*a*) As emphasized by Bergougnoux *et al.* (2003), polydispersity can be a significant effect in the spreading of a sedimentation front. In our own experiments, there is about a 10% polydispersity in the particle radius, leading to a variation in the falling velocities $\delta V_0/V_0 \approx 0.2-0.3$. At times t, polydispersity will spread an initially sharp front over heights comparable to $t\delta V_0$ while a constant diffusivity would create spreading on a scale $\sqrt{tD} \sim \sqrt{td\Delta V}$. The latter is larger than the former up to times $t \sim d\Delta V/(\delta V_0)^2$ or, in terms of the total sedimentation time, $tV_0/h \sim (d/h)(\Delta V/\delta V_0)(V_0/\Delta V_0)$. For very thick cells, with larger initial ΔV fluctuations, polydispersity is a smaller effect on the evolving stratification away from the sediment front. For thin cells, the polydispersity contribution to spreading can be very significant, but the critical stratification in such thin cells is much larger, so velocity fluctuations in measurement windows far from the front are typically measured to be close to the Poisson predictions. In our experiments, with h/d typically $O(20-50)$ and ΔV fluctuations comparable to V_0, this crossover time is on the same order as the total experiment time. Thus, while we conclude that a significant part of the evolution of our observed spreading fronts is attributable to effective diffusion, this estimate indicates that polydispersity is also fundamentally important. Such spreading due to polydispersity further increases the stratification in the measurement window.

(*b*) Both the diffusivity and the falling velocity depend on particle concentration (as in, e.g. Batchelor 1972; Martin, Rakotomalala & Salin 1994), these dependences being especially important near the front. An advection–diffusion model with diffusivity dependent on both concentration and stratification as for the results of the present section was found (Mucha & Brenner 2003) to agree with our simulations; steadily falling concentration profiles obtained from that model, including hindered settling, indicate dynamically important stratifications over $3d$ below the $\phi = 0.9\phi_0$ point of the front for a wide range of experimentally studied parameters. That same dependence of the diffusivity leads to front thicknesses which scale with time like $t^{5/7}$ (E. J. Hinch, private communication), providing a possible description of the front spreading in the simulations of Bergougnoux *et al.* (2003) as well.

5.3.2. *Occupancy statistics*

The simple form of the isotropic $S(q)$ model (5.10) and its predictions of correlations in the particle positions could be tested in experiments. Such correlations have previously been observed by Lei *et al.* (2001), who demonstrate that initially Poisson number fluctuations are suppressed over time in their experiments, by directly measuring the number occupancy variance σ^2 in finite test volumes with an average number of particles $\langle N\rangle$. We replicate these measurements on our simulation data, calculating σ^2 at each $\langle N\rangle$ by sampling 10 000 randomly positioned cubic test volumes in a single time frame at a height $z \approx h/3$ above the bottom of the cell. Averaging together such results from $O(20)$ nearby time frames (over a total time interval

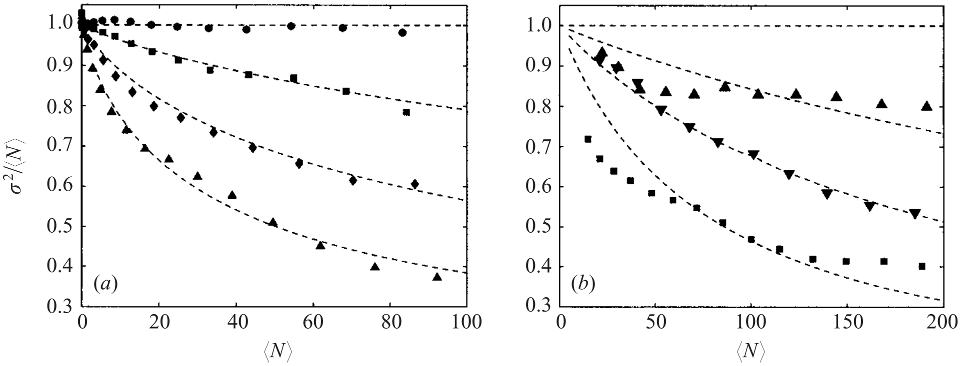

FIGURE 9. Number occupancy variances, σ^2, versus average number of particles in the test volume, $\langle N\rangle$. (*a*) Simulation data from cubic test volumes in four different regimes (selected from the simulation data presented in figure 7), where $\Delta V_z/V_0 \approx 0.99$ (●), 0.86 (■), 0.57 (◆), and 0.42 (▲). The dashed lines are the result of numerical quadrature of (5.15) over spherical test volumes with $S(q)$ given by the isotropic form (5.10) for different parameters. The $S(q)$ parameters used in the two most stratified cases are well-approximated by $\alpha d^4 = A\beta V_0\phi d^4/(Da^2) \approx (8\pi\beta/\beta_{crit})^{8/5}$, in agreement with the predicted large stratification scaling. (*b*) Comparison of the non-Poisson experimental data from figure 3 of Lei *et al.* (2001) with occupancy statistics calculated from (5.10), (5.15) over rectangular box test volumes with constant thin dimension equal to the light sheet thickness in the experiments, for various α values as described in the text.

of order $d/\Delta V_z$, in which ΔV only changes slightly) gives occupancy variances for different $\langle N\rangle$-sized test volumes at different times like the points plotted in figure 9(*a*), obtained from simulations with decaying ΔV. We observe the suppression of large-scale number fluctuations as the simulations progress, similar to the experiments of Lei *et al.* (2001) (i.e. as in figure 3 of Lei *et al.* 2001, reproduced here in figure 9*b*). These number occupancy fluctuations are related to the structure factor by (cf. Lei *et al.* 2001)

$$\frac{\sigma^2}{\langle N\rangle} = 1 + \frac{1}{\theta_0(2\pi)^3}\int \mathrm{d}\boldsymbol{q}\ [\theta(-\boldsymbol{q})]^2\,[S(\boldsymbol{q})-1], \tag{5.15}$$

where $\theta(\boldsymbol{r})$ is an indicator function for the test volume, unity inside and zero otherwise, $\theta(\boldsymbol{q}) = \int \mathrm{d}\boldsymbol{r}\,\theta(\boldsymbol{r})\mathrm{e}^{-\mathrm{i}\boldsymbol{q}\cdot\boldsymbol{r}}$, and $\theta_0 = \theta(\boldsymbol{q}=\boldsymbol{0})$ is the volume of the test region.

Substituting (5.10) into (5.15), computing the resulting isotropic integral (for spherical test volumes) by numerical quadrature, gives the dashed curves plotted in figure 9(*a*) for different values of $\alpha = A\beta V_0\phi/(Da^2)$. By the large stratification scalings above, and $\beta_{crit}d = [\phi(d/a)^3]^{-1/2}$, this parameter should scale like $\alpha \sim (q^*)^4 \sim d^{-4}(\beta/\beta_{crit})^{8/5}$. This scaling is confirmed by the two strongest-stratified occupancy fluctuations considered in figure 9(*a*), which were each fitted with $\alpha d^4 \approx (8\pi\beta/\beta_{crit})^{8/5}$, consistent with both the measured stratification β and the observed velocity fluctuations (with ΔV_z values 42% and 57% of their Poisson predictions). The least-stratified data accompanies fluctuations $\Delta V_z \approx 0.99\Delta V_{\mathrm{Poisson}}$, and is well fitted by the $\alpha = 0$, $S(q) = 1$, $\sigma^2/\langle N\rangle = 1$ independent homogeneous result. Meanwhile, the weakest of the $\sigma^2/\langle N\rangle \neq 1$ cases considered in figure 9(*a*) appears to be in the intermediate regime influenced by both sidewalls and stratification, with $\Delta V_z \approx 0.86\Delta V_{\mathrm{Poisson}}$, fitted by an α slightly larger than the ‘8π’ scaling used for the more stratified cases.

For comparison, occupancy statistics data from the experiments of Lei *et al.* (2001) (figure 3 therein) are reproduced in figure 9(*b*) and compared with (5.15) for rectangular box test volumes with constant thin dimension (of the thickness of the light sheet, 0.35 mm). Fitting the data to the theory implies stratifications (assuming the '8π' scaling observed above) $\beta/\beta_{\text{crit}} \approx 6.5, 22, 68$. With $N_d = \phi(d/a)^3 \doteq 440\,000$, the critical stratification of the Lei *et al.* (2001) experiments is $\beta_{\text{crit}} d \approx 1/660$. The presumed stratifications in figure 9(*b*) thus go up to $\beta d \approx 1/10$. While such local stratifications would perhaps go unnoticed in their $h = 4d$ cells without directly searching for them, they might perhaps be measured directly in future experiments.

These excellent comparisons obtained between (5.10), (5.15) and the occupancy variances directly measured both in simulations and in the Lei *et al.* (2001) experiments indicates that our steady isotropic $S(q)$ model contains the essential dependence on stratification necessary to explain a wide body of computational and experimental results.

5.3.3. *Velocity fluctuations*

Our results suggest that for measurements showing velocity fluctuations below the calculation of the uniform distribution presented in § 2 a stratification above the critical value $\beta_{\text{crit}} d \sim 1/\sqrt{\phi(d/a)^3}$ must have developed. We have previously demonstrated that this idea quantitatively agrees with our own experiments in thick cells (Tee *et al.* 2002). Here we explore whether this is a consistent interpretion of previous experiments.

Clearly, without exploring details of previous experiments (e.g. the mixing procedure and polydispersity), it is impossible for us to definitively deduce their stratification. However, the constant diffusion model, validated on our own data in § 5.3.1, provides a lower bound on the stratification that probably existed in many dilute experiments.

To test whether stratification has played a role in previous experiments, we employ a constant-diffusivity error function for the spreading of the sediment front to estimate the time, t_{crit}, in the experiments when the stratification in the imaging window is sufficient to suppress velocity fluctuations. This time was extracted by taking the solution $\phi(z, t)$ for the particle concentration in the experimental cell in question (with the diffusivity set by the cell size and volume fraction as outlined above), and then solving for the time t_{crit} when the gradient exceeds the critical stratification $\frac{1}{2}\beta_{\text{crit}}$ at the location of the imaging window:

$$\partial_z \phi(z = h/3, t_{\text{crit}}) = \frac{\beta_{\text{crit}}}{2}.$$

The imaging window is assumed to be located near $z = h/3$, where h is the initial height of the sediment (P. N. Segrè, private communication). Solving this equation using the physical parameters of various previous experiments, we use this as a simple estimate for the time t_{crit} at which stratification becomes important in the experiment. We also solve for the time t_1 when the gradient reaches β_{crit}. These times are then compared with t_{expt}, the time it takes the sediment front to reach an imaging window at $z = h/3$.

The results of these calculations for the Segrè *et al.* (1997), Nicolai & Guazzelli (1995), and Guazzelli (2001) experiments are summarized in table 1. At the higher volume fractions and larger cells where the measured velocity fluctuations are below the calculation of the uniform distribution, the estimates indicate that the stratification in the imaging window probably exceeds the critical stratification early in the experiment. In contrast, the stratification in the experiments where the velocity fluctuations are accurately predicted by the uniform Poisson distribution formulae stays below the critical stratification for most of the experimental time. These results

ϕ	Obs. $\Delta V_z/V_0$	Poisson (2.1)	h/a	t_{crit}	Obs. ΔV_z/Poisson	$t_{\mathrm{crit}}/t_{\mathrm{expt}}$	t_1/t_{expt}
Nicolai & Guazzelli (1995):							
5×10^{-2}	0.67	1.15	1269	363	0.58	0.43	0.48
5×10^{-2}	0.62	1.62	1269	162	0.38	0.19	0.22
5×10^{-2}	0.60	1.99	1269	88	0.30	0.10	0.12
5×10^{-2}	0.73	2.29	1269	55	0.32	0.065	0.072
Segrè *et al.* (1997):							
1×10^{-4}	0.13	0.139	39077	23708	0.94	0.91	0.93
2×10^{-4}	0.12	0.139	12821	7725	0.87	0.90	0.93
3×10^{-3}	0.28	0.374	12821	7310	0.75	0.86	0.89
3×10^{-2}	0.56	0.773	6410	3616	0.72	0.85	0.92
6×10^{-4}	0.167	0.240	12821	7387	0.70	0.86	0.89
3×10^{-2}	0.75	1.18	12821	6141	0.64	0.72	0.76
6×10^{-4}	0.19	0.339	39077	22097	0.56	0.85	0.87
2×10^{-2}	0.53	0.965	12821	6390	0.55	0.75	0.79
3×10^{-3}	0.25	0.536	12821	6698	0.47	0.78	0.82
1×10^{-2}	0.44	0.979	12821	6001	0.45	0.70	0.74
2×10^{-2}	0.556	1.39	12821	5523	0.40	0.65	0.69
4×10^{-3}	0.244	0.619	12821	6547	0.39	0.77	0.80
3×10^{-2}	0.589	1.70	12821	5220	0.35	0.61	0.65
5.5×10^{-2}	0.75	2.30	12821	4735	0.33	0.55	0.60
6×10^{-4}	0.16	0.759	25641	6208	0.211	0.36	0.39
Guazzelli (2001):							
5×10^{-4}	0.35	0.50	2703	159	0.70	0.088	0.095

TABLE 1. Previously reported experimental ΔV_z^2, with their respective homogeneous Poisson estimates (2.1), compared to an estimate of the critical stratification time of the experiment, t_{crit} (in Stokes times), when the estimated stratification β reaches $\frac{1}{2}\beta_{\mathrm{crit}} = \frac{1}{2}(d\sqrt{N_d})^{-1}$. The critical time estimate is made by assuming that measurements are taken at a height $z \approx \frac{1}{3}h$ above the bottom of the cell, and that the sediment front spreads with constant vertical diffusivity $D \approx \frac{1}{2}d\Delta V_{\mathrm{Poisson}}$ as it falls (ignoring corrections due to flux conditions at the cell bottom). This time is then compared with the time it takes the dilute front to reach the measurement height, $t_{\mathrm{expt}} = 2h/(3a)$. For comparison, we also include t_1/t_{expt}, where t_1 is the time to reach $\beta = \beta_{\mathrm{crit}}$ in this simplified estimate for the spreading of the front, where the stratification has already significantly decreased the fluctuations.

suggest that it is reasonable to believe that the critical stratification was exceeded in previous dilute experiments.

A further comparison can be made by calculating how a presumed stratification might affect the Segrè *et al.* (1997) measurements that led to the $\Delta V/V_0 \sim \phi^{1/3}$ conjecture. Figure 10 replots the Segrè *et al.* (1997) data for the vertical fluctuations compared with both the Poisson prediction and the predictions of the stratification model for $\beta d = 0.01$ and $\beta d = 0.05$. These are extremely small stratifications, corresponding to differences of hundreds of particles across regions the size of the small dimension d which contain $O(10^4)$ particles when $\phi = 0.01$. These hypothesized stratifications capture the trends of the experimental data exceedingly well, demonstrating the potentially large effect of very small stratifications.

Additionally, during the writing of the present paper we became aware of a study by Ladd (2002), which shows some conditions where velocity fluctuations decrease in time in lattice-Boltzmann simulations of sedimentation. In particular, those simulations also conclude that the container bottom is necessary in order to decrease velocity

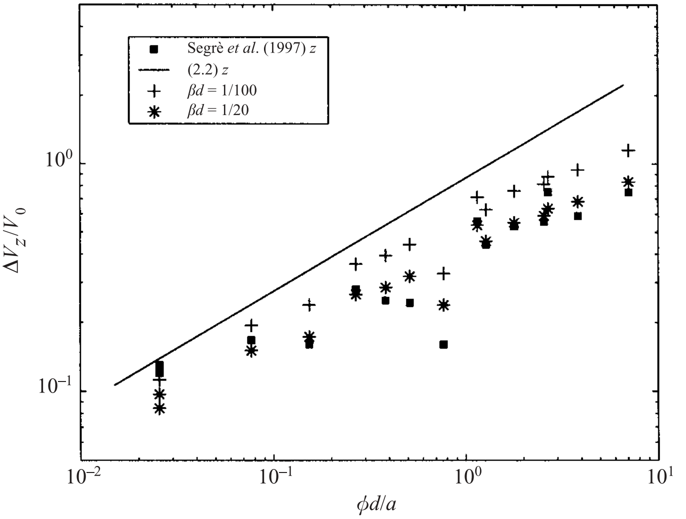

FIGURE 10. Comparison of midplane Poisson estimate (2.2) with ΔV_z experimental results from figure 3 of Segrè *et al.* (1997), and estimates (cf. figure 3) modified by stratifications of $\beta d = 1/100$ and $\beta d = 1/20$ also including depth-averaging of the velocity standard deviations and finite volume fraction effects (Segrè *et al.* 2001).

fluctuations below those of the independent-Poisson Caflisch & Luke scaling. There are important differences between Ladd's simulations and those of the present paper, most notably the fact that the volume fractions there are ≈ 0.13 with particle Reynolds numbers $\sim O(0.1)$, the former introducing stronger self-sharpening and other non-dilute effects, the latter changing the single particle velocity field from the $u \sim r^{-1}$ law that underlies the present study. Despite these important differences, Ladd's results are in reasonable agreement with the stratification suppression of velocity fluctuations presented here. The deviation from the Caflisch & Luke (1985) scaling in Ladd's simulations occurs when $\Delta V \gtrsim V_{sed}$. The largest simulations presented in Ladd (2002), wherein four-fold decrease in the velocity variances is observed, are of $N \approx 35\,000$ particles, with $N_d \approx 14\,400$ yielding $\beta_{crit} d \sim 1/120$ in (5.3). Meanwhile, the least-squares fit across the measurement window (figure 3 of Ladd 2002) indicates a stratification $\beta \approx 1/(13\,000a)$, corresponding to $(d = 48a)$ $\beta d \approx 1/220$, with local stratifications in the figure over distances $\sim d$ up to perhaps $O(10)$ larger. For comparison, our dilute-limit creeping flow simulations indicate (see figure 7) a two-fold decrease in the velocity variances at $\beta \approx 3\beta_{crit}$, and a four-fold decrease at $\beta \approx 16\beta_{crit}$.

Lastly, we have recently become aware of new experiments and simulations by Bergougnoux *et al.* (2003) which study the spreading of the sediment front in detail, including the effects of polydispersity. The numerical Poisson estimate for square cells (§ 2) predicts $\Delta V_z \approx 1.2V_0$ velocity fluctuations in the centre of their $\phi = 0.003$, $d/a \approx 1342$ experiments, wherein the observed steady fluctuations are $\Delta V_z \approx 0.5V_0$ after an initial transient. For comparison, the model presented herein predicts that the critical stratification above which we expect velocity fluctuations to become suppressed is as small as $\frac{1}{2}\beta_{crit} d = [\phi(d/a)^3]^{-1/2} \doteq 1/5385$; the local stratification needed to suppress ΔV by the observed 0.5/1.2 factor is $\beta d \approx 1/70$. The measured concentrations in their figure 1 indicate local stratification of this order in the measurement window at least as early as $O(700)$ Stokes times after the end of mixing, well inside the interval when their measured velocity fluctuations appear roughly constant, but not as early as the $O(200)$ Stokes times at which their measured fluctuations are already this small.

As pointed out by E. J. Hinch (private communication), the Bergougnoux *et al.* (2003) experimental cells have a fundamentally different geometry than that considered here: their experimental cells, at $d \times d \times 2d$, are of a significantly smaller h/d aspect ratio than the $d \ll h$ cells considered here, so two of the fundamental assumptions of our model do not apply to their case. First, concentration profiles in measurement windows apparently far from the front do not remain locally linear at length scales larger than the correlation length. Second, the turnover time $\ell/\Delta V$ in the Bergougnoux *et al.* (2003) experiments is comparable to the h/V_0 sedimentation time, breaking the temporal scale separation that underlies all of the arguments presented herein.

This points to the intriguing idea that there are two different limits to the velocity fluctuations problem, determined by the aspect ratio of the cell. The model outlined herein operates at large h/d aspect ratios, when the correlation length is smaller than the length scale of any developed stratification, and the swirl turnover time is short compared to the sediment transport time scale so that the stochastic continuum model can be applied. A model that operates at smaller h/d aspect ratios remains to be worked out. It seems clear that in this limit, direct advection of density fluctuations (Hinch 1988) will play an important role.

6. Conclusions

The results reported here suggest a picture for velocity fluctuations in sedimentation that is quantitatively consistent with previously reported simulations and experiments. The model implies that velocity fluctuations are non-universal, with dependence not only on the cell depth but also on the local stratification of the particles. When $\Delta V \lesssim V_0$, the fluctuations are controlled by the cell depth until a critical stratification develops at the imaging window, after which the fluctuations may decay slowly. When $\Delta V \gtrsim V_0$, the spreading of the sediment front is greatly enhanced, and rapid, persistent decay of the fluctuations can occur because the local stratification in the measurement window is continually increasing. Below the critical stratification, the velocity fluctuations are controlled by the small cell dimension, $\Delta V \sim V_0\sqrt{\phi d/a}$, with the prefactors accurately calculated from the independent Poisson distribution. Above the critical stratification, the fluctuations scale like $\Delta V \sim V_0\phi^{2/5}(\beta a)^{-1/5}$. Along with these changes in the velocity fluctuations, the correlation length transitions from being set by the cell depth at small stratifications to $\ell \sim a\phi^{-1/5}(\beta a)^{-2/5}$ above the critical stratification. The dependence of ΔV on β has been directly and successfully tested in our simulations (figure 7), while the steady isotropic $S(q)$ model (5.10) compares favourably with the simulations and with the Lei *et al.* (2001) experiments (figure 9). The present model for velocity fluctuations in sedimentation quantitatively agrees with our numerical simulations and experiments, and also provides a consistent interpretation of previous results for large h/d aspect ratios.

There remain, however, many aspects of the model that are amenable to further quantitative experimental tests. For example, fluidized beds offer the possibility of directly comparing velocity fluctuations with a time-independent concentration gradient. Also significant is the possible extension of these results to higher volume fractions, where a number of effects ignored here become important. Segrè *et al.* (2001) demonstrated that experimentally measured velocity fluctuations across all volume fractions can be connected to those measured in the dilute Segrè *et al.* (1997) experiments; the physically motivated modifications for dense systems being in terms of well-known empirical relationships for hindered settling, effective viscosity, and the structure factor of hard spheres. The idea of applying such empirical corrections to the present, dilute model may hold the possibility of quantitatively describing velocity fluctuations across all volume fractions, hopefully yielding improved continuum models. We suggest that future experiments and simulations should attempt to test such connections between dense sedimentation behaviour and the dilute model presented here. Of course, a number of other effects also need to be further explored, including but not limited to polydispersity, orientations of non-spherical particles, non-zero Reynolds numbers, and the breakdown of the time scale separation at smaller h/d aspect ratios.

From our point of view, the essential conclusion of this work is that the velocity fluctuations in sedimentation at low volume fractions are extremely sensitive to small physical effects. The velocity fluctuations are driven by number density fluctuations, which scale with the square root of volume. However, any external body force necessarily scales linearly with volume. Hence, the relative external body force necessary to overcome the fluctuations, if oriented to suppress those fluctuations, decreases with increasing cell size. The sensitivity of sedimentation to such small effects, coupled with the inevitable low-Reynolds-number flow dependence on the long-range properties of the particle distribution and the shape of the container containing the flow, makes the possibility of a locally generated universal screening mechanism unlikely.

The theoretical and computational research presented here was supported by the NSF through the Division of Mathematical Sciences (M. P. B.), including a postdoctoral fellowship (P. J. M); the experimental work was supported by NASA (NAG3-2376). We thank P. M. Chaikin for critical input; L. Cipelletti and S. Manley for extensive discussions about their experiments; J. W. M. Bush, E. Guazzelli, E. J. Hinch, T. Peacock, V. Prasad and P. N. Segrè for useful conversations; and E. M. Tory for pointing out the Kermack *et al.* (1929) reference.

Appendix A. Velocity fields and numerical methods with sidewalls

Effects due to the presence of no-slip walls can be studied in an otherwise homogeneous sediment via systems with a pair of infinite sidewalls separated by a distance d along the x-coordinate, with periodic boundary conditions in the other two dimensions, y and z, of periodic length w and h, respectively. Calculation of the advection Green's function in such systems proceeds by Fourier series expansion in the y and z dimensions, $\boldsymbol{S}(\boldsymbol{r},\boldsymbol{r}_0)=\sum_{\boldsymbol{k}}\hat{\boldsymbol{S}}\exp\{\mathrm{i}ly+\mathrm{i}mz\}$, with the summation over two-dimensional wavevectors $\boldsymbol{k}=(l,m)$ (not integers). Notating velocity components by $\boldsymbol{S}=(u,v,w)$ (the Green's function component w not to be confused with the y-coordinate periodic length w, different meanings hopefully clear herein from context), and remaining derivatives with respect to x by subscripts, the incompressible Stokes equations for a unit upward point force at $\boldsymbol{r}_0=(X,0,0)$ become

$$\left.\begin{aligned}&\hat{p}_x/\eta=\hat{u}_{xx}-(l^2+m^2)\hat{u}, \qquad \mathrm{i}l\hat{p}/\eta=\hat{v}_{xx}-(l^2+m^2)\hat{v},\\ &\mathrm{i}m\hat{p}/\eta=\hat{w}_{xx}-(l^2+m^2)\hat{w}+1/(\mathscr{A}\eta)\delta(x-X), \qquad \hat{u}_x+\mathrm{i}l\hat{v}+\mathrm{i}m\hat{w}=0,\end{aligned}\right\} \tag{A 1}$$

with $(\hat{u}, \hat{v}, \hat{w}) = \mathbf{0}$ along the sidewalls, $x = 0, d$, and $\mathscr{A} = wh$ the cross-sectional area of the cell. Summing multiples and derivatives to eliminate the velocities via incompressibility, the pressure equation becomes $\hat{p}_{xx} - (l^2 + m^2)\hat{p} = (\mathrm{i}m/\mathscr{A})\delta(x - X)$. Since the forcing appears via a Dirac delta, it is convenient to solve separately for the homogeneous solutions to the left and right of the source position, connected by appropriate jump conditions across $x = X$. The pressure on each side is a linear combination of $\sinh(kx)$ and $\cosh(kx)$, $k = \sqrt{l^2 + m^2}$, and the velocity boundary condition at $x = 0$ gives, on the left,

$$\left.\begin{aligned}
\hat{u}_L &= A_1 \sinh(kx) + x[B_L \cosh(kx) + C_L \sinh(kx)],\\
\hat{v}_L &= A_2 \sinh(kx) + (\mathrm{i}lx/k)[C_L \cosh(kx) + B_L \sinh(kx)],\\
\hat{w}_L &= A_3 \sinh(kx) + (\mathrm{i}mx/k)[C_L \cosh(kx) + B_L \sinh(kx)],\\
\hat{p}_L &= 2\eta[B_L \cosh(kx) + C_L \sinh(kx)],
\end{aligned}\right\} \tag{A 2}$$

with $B_L = -kA_1$ and $C_L = -\mathrm{i}lA_2 - \mathrm{i}mA_3$. The A_j coefficients depend on the source position X and the wavevector $\boldsymbol{k}$. Similarly, the boundary condition at $x = d$ gives, on the right,

$$\left.\begin{aligned}
\hat{u}_R &= A_4 \sinh(kx') - x'[B_R \cosh(kx') + C_R \sinh(kx')],\\
\hat{v}_R &= A_5 \sinh(kx') + (\mathrm{i}lx'/k)[C_R \cosh(kx') + B_R \sinh(kx')],\\
\hat{w}_R &= A_6 \sinh(kx') + (\mathrm{i}mx'/k)[C_R \cosh(kx') + B_R \sinh(kx')],\\
\hat{p}_R &= 2\eta[B_R \cosh(kx') + C_R \sinh(kx')],
\end{aligned}\right\} \tag{A 3}$$

with $x' \equiv d - x$, $B_R = kA_4$, $C_R = -\mathrm{i}lA_5 - \mathrm{i}mA_6$, and again $A_j = A_j(\boldsymbol{k}, X)$. The A coefficients are determined by the jump conditions imposed at $x = X$. The transforms $\hat{u}$, $\hat{v}$, $\hat{w}$, and $\hat{p}$ are necessarily continuous across the jump. Integrating (A 1), $\hat{u}_x$ and $\hat{v}_x$ are also continuous, while $\hat{w}_x$ and $\hat{p}_x$ have finite jumps at $x = X$: $[\hat{w}_x] = -1/(\mathscr{A}\eta)$, and $[\hat{p}_x] = \mathrm{i}m/\mathscr{A}$. For given $\boldsymbol{k}$ and X, these jump conditions and (A 2), (A 3) give eight non-independent linear equations in the six A_j unknowns, the solution for which is straightforward, albeit tedious, yielding

$$A_1 = \mathrm{i}m\frac{X\mathrm{e}^{4kd-kX} + [4kd(d - X)\sinh(kX) - 2X\cosh(kX)]\,\mathrm{e}^{2kd} + X\mathrm{e}^{kX}}{2k\mathscr{A}\eta[\mathrm{e}^{4kd} - (4k^2d^2 + 2)\mathrm{e}^{2kd} + 1]}, \tag{A 4}$$

$$\begin{aligned}
A_2 = lm\{&(-1 - kX)\mathrm{e}^{6kd-kX} + [4kd\sinh(kX) + 4k^2dX\cosh(kX) + (1 - kX\\
&- 2k^2d^2)\mathrm{e}^{kX} + (2 + 2kX + 6k^2d^2)\mathrm{e}^{-kX}]\mathrm{e}^{4kd} - [4kd\sinh(kX) + 4k^2dX\cosh(kX)\\
&+ (2 - 2kX + 6k^2d^2)\mathrm{e}^{kX} + (1 + kX - 2k^2d^2)\mathrm{e}^{-kX}]\mathrm{e}^{2kd} + (1 - kX)\mathrm{e}^{kX}\}\\
&/\{2k^3\mathscr{A}\eta[\mathrm{e}^{6kd} - (4k^2d^2 + 3)(\mathrm{e}^{4kd} - \mathrm{e}^{2kd}) - 1]\},
\end{aligned} \tag{A 5}$$

$$\begin{aligned}
A_3 = \{&(2k^2 - m^2 - m^2kX)\mathrm{e}^{6kd-kX} + [4m^2kd\sinh(kX) + 4m^2k^2dX\cosh(kX)\\
&+ (m^2 - 2k^2 - m^2kX - 2m^2k^2d^2)\mathrm{e}^{kX} + (2m^2 - 4k^2 + 2m^2kX + 6m^2k^2d^2\\
&- 8k^4d^2)\mathrm{e}^{-kX}]\mathrm{e}^{4kd} + [-4m^2kd\sinh(kX) - 4m^2k^2dX\cosh(kX) + (4k^2 - 2m^2\\
&+ 8k^4d^2 + 2m^2kX - 6m^2k^2d^2)\mathrm{e}^{kX} + (2k^2 - m^2 - m^2kX + 2m^2k^2d^2)\mathrm{e}^{-kX}]\mathrm{e}^{2kd}\\
&+ (-2k^2 + m^2 - m^2kX)\mathrm{e}^{kX}\}/\{2k^3\mathscr{A}\eta[\mathrm{e}^{6kd} - (4k^2d^2 + 3)(\mathrm{e}^{4kd} - \mathrm{e}^{2kd}) - 1]\},
\end{aligned} \tag{A 6}$$

$$A_4 = \mathrm{i}m\frac{kdX(\mathrm{e}^{kd+kX} - \mathrm{e}^{3kd-kX}) + (d - X)\sinh(kX)(\mathrm{e}^{kd} - \mathrm{e}^{3kd})}{k\mathscr{A}\eta[\mathrm{e}^{4kd} - (4k^2d^2 + 2)\mathrm{e}^{2kd} + 1]}, \tag{A 7}$$

$$\begin{aligned}A_5 = -lm\{&[(1+kd)\sinh(kX) - kX\cosh(kX) + k^2dX\mathrm{e}^{-kX}]\mathrm{e}^{5kd} + [(2k^2dX \\ &- 8k^2d^2 - 2)\sinh(kX) + 2kX\cosh(kX)]\mathrm{e}^{3kd} + [(1-kd)\sinh(kX) - kX\cosh(kX) \\ &- k^2dX\mathrm{e}^{kX}]\mathrm{e}^{kd}\}/\{k^3\mathscr{A}\eta[\mathrm{e}^{6kd} - (4k^2d^2+3)(\mathrm{e}^{4kd} - \mathrm{e}^{2kd}) - 1]\},\end{aligned} \qquad (\mathrm{A}\,8)$$

$$\begin{aligned}A_6 = -\{&[(2k^2 - m^2 - kdm^2)\sinh(kX) + m^2kX\cosh(kX) - m^2k^2dX\mathrm{e}^{-kX}]\mathrm{e}^{5kd} \\ &+ [(2m^2 - 2m^2k^2dX + 8m^2k^2d^2 - 8k^4d^2 - 4k^2)\sinh(kX) - 2m^2kX\cosh(kX)]\mathrm{e}^{3kd} \\ &+ [(m^2kd + 2k^2 - m^2)\sinh(kX) + m^2kX\cosh(kX) + m^2k^2dX\mathrm{e}^{kX}]\mathrm{e}^{kd}\} \\ &/\{2k^3\mathscr{A}\eta[\mathrm{e}^{6kd} - (4k^2d^2+3)(\mathrm{e}^{4kd} - \mathrm{e}^{2kd}) - 1]\}.\end{aligned} \qquad (\mathrm{A}\,9)$$

The resulting advection Green's function, $\boldsymbol{S}(\boldsymbol{r}, \boldsymbol{r}_0)$, can be reconstructed to arbitrary precision by calculation of the Fourier sums.

The no-net-flow condition in this geometry is expressed in the $\boldsymbol{k}=\boldsymbol{0}$ terms, modifying (A 1) with a vertical pressure gradient: $\hat{u}=0$, $\hat{v}=0$, $\hat{p}_x=0$, and $\hat{w}_{xx}+1/(\mathscr{A}\eta)\delta(x-X)+\nabla P=0$, where ∇P is a viscosity-normalized pressure gradient driving a backflow. The $\boldsymbol{k}=\boldsymbol{0}$ contribution then becomes $\hat{w}_L = A_Lx + A_Bx(d-x)$, $\hat{w}_R = A_R(d-x) + A_Bx(d-x)$, where $A_L = (d-X)/(d\mathscr{A}\eta)$, $A_R = X/(d\mathscr{A}\eta)$, $A_B = -3X(d-X)/(d^3\mathscr{A}\eta)$.

The above method of solution yields a doubly periodic (in y and z) incompressible Stokes solution that obeys the no-slip boundary conditions at the sidewalls term-by-term in the Fourier sum. The left solution summation is absolutely convergent to the left of the forcing, the right solution is similarly convergent to the right of the forcing, with each solution becoming only conditionally convergent along the $x=X$ plane. In practice, of course, the two-dimensional Fourier sum is truncated at some order, say, summing over the N_k-by-N_k terms in the $N_k\pi/w \times N_k\pi/h$ rectangle centred at the wavevector-space origin. This truncation effectively smooths the spatial extent of the point force. The resulting flow is the incompressible Stokes flow for this smoothed forcing, and continues to obey the no-slip boundary conditions at the sidewalls. If finer resolution of the short-range point-force interaction is desired, the smoothing due to this two-dimensional Fourier representation can be corrected at short ranges into simple known functional interactions, such as a Stokeslet plus backflow. Additional short-range interactions, such as those that might approximate an excluded volume or attractive interactions can be similarly added here by standard particle simulation techniques. In most of the simulation results presented here, the Fourier-truncated sidewall point-force solutions were used without additional interactions or short-range corrections.

The A_j field coefficients above motivate efficient $O(N\log N)$ evaluation (for N particles, at fixed N_k) by a 'sort-and-sweep' algorithm. After an initial $O(N\log N)$ sort of the particle x-positions in a given time step, the first $O(N)$ sweep starts at the left wall, looping over the sorted particle index, calculating responses from the total 'right' coefficients (A_4, A_5, A_6) of the already-swept sources, then adding the current sources to the field coefficients before proceeding to the next particle to the right. The second $O(N)$ sweep returns from right to left with the 'left' coefficients (A_1, A_2, A_3).

The above velocity fields and sort-and-sweep algorithm allows dilute-limit simulations in cells bounded by a pair of no-slip sidewalls in one dimension, periodic in the other two dimensions, of up to $O(4\times10^6)$ particles on a standard PC or workstation, with computing times of $O(10-1000)$ hours, depending on the Fourier truncation N_k and on the long-time nature of the desired quantities. Free-slip container bottoms and tops are added by simple lowest-order images of the dilute point forces, which is accurate for heights larger than the cell depth d. While these dilute-limit point-force calculations ignore important hydrodynamic effects at higher volume fractions (as, e.g. handled in the simulations of Brady & Bossis 1988, Ladd 1994 and Sangani & Mo 1996), the form of the interactions treated here allows the simulation of far greater numbers of particles, in order to directly address the conjecture that the correlation length in sedimentation is saturated at a 'universal' $O(10-20)$ mean interparticle spacings.

Appendix B. Vertically homogeneous sedimentation

We detail here a number of ways in which the statistically steady state observed in our vertically periodic, dilute-limit simulations (§ 3 and Appendix A) are well-described by an independent Poisson particle distribution. As discussed in § 3, the swirls observed in the simulations (figure 1) are visually similar to those observed experimentally (Segrè *et al.* 1997), with statistically steady velocity fluctuations (e.g. figure 2) in agreement with the Poisson prediction (2.2) at the same truncation in the numerical method, with values similar to (2.3). In this Appendix, we demonstrate that the spatial dependence of the velocity fluctuations, the resulting mean-squared relative displacements, and higher-order velocity statistics including the fluctuations of the fluctuations are all in agreement with independent Poisson particle distributions.

Everything below changes when the vertically homogeneity is broken. At stratifications below the critical stratification, the local particle distribution remains essentially independent Poisson, and the results below continue to hold. In contrast, the statistically steady particle distribution is significantly non-Poisson above the critical stratification. The resulting structure factor, perhaps as modelled in (5.10), must then be considered in making predictions about the spatial dependence of the fluctuations or about the fluctuations of the fluctuations. On the other hand, the mean-squared relative displacements and the resulting hydrodynamically induced diffusivities should continue to obey $D \sim \ell \Delta V$ in a given region provided that the swirl size ℓ remains significantly smaller than the height over which the stratification changes appreciably, so that the spatial region accessed by a particle in a swirl during its lifetime remains sufficiently similar, statistically speaking; otherwise, the fluctuating particle motions become significantly more complicated.

B.1. *Spatial dependence of velocity fluctuations*

The spatial dependence of the velocity variance on the interwall coordinate, x, agrees with the Poisson prediction in vertically periodic systems. Figure 11 compares the x-dependence of C_α in the simulations and the independent uniform prediction, with excellent agreement. Figure 11(a) compares the variances of each velocity component in a simulation of 1 024 000 particles without any time averaging, and slight quantitative variations from the uniform distribution are notable at this time instant. When time averaged (as in figure 11b) the agreement is extremely good.

B.2. *Mean-squared relative displacements*

Figure 12 shows the mean-squared relative displacements of the particles in vertically periodic simulations as a function of time for different particle numbers and cell dimensions. Figure 12(a) shows that these mean-squared displacements make a transition from ballistic to diffusive behaviour at a time that varies according to the particle number and cell size. Figure 12(b) shows that all of the data collapse onto single curves for each velocity component when the displacements are scaled by the cell depth and the characteristic time is scaled by $\sqrt{d/n}/(aV_0)$. This demonstrates that the correlation length for the simulations is indeed the cell depth d, and the characteristic

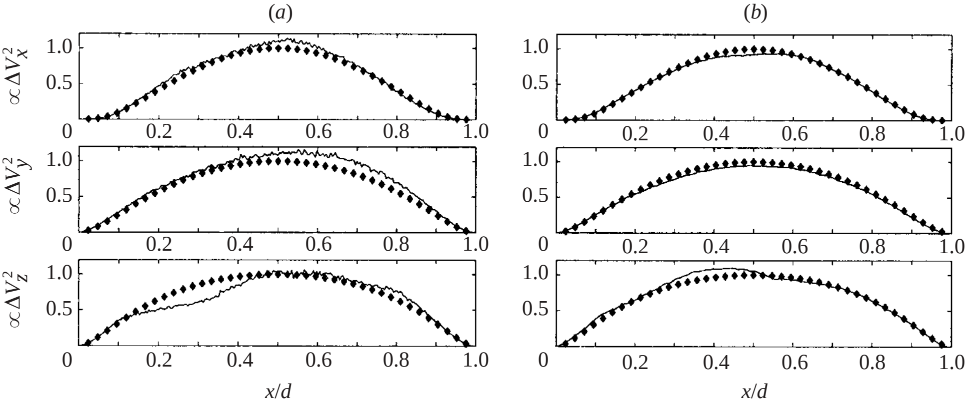

FIGURE 11. Comparison of velocity fluctuations observed in $4d = w = h$ sidewall $N_k = 15$ simulations (——) with spatial dependence predicted by the independent-Poisson estimate at the same interaction truncation (◆). Observed and predicted values have been scaled by the predicted midplane value: (*a*) a single frame from an $N = 1\,024\,000$ simulation, (*b*) averaging over 100 time steps from an $N = 128\,000$ simulation.

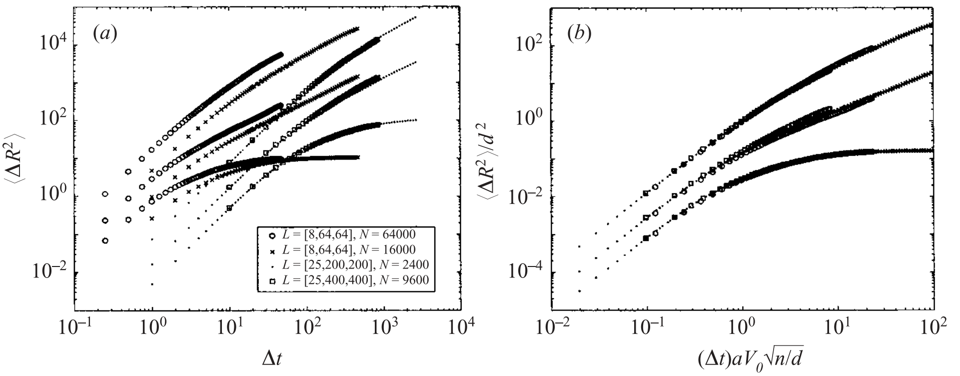

FIGURE 12. Mean-squared relative displacements, $\langle \Delta R^2 \rangle$, in each direction vs. time, Δt, for sidewall simulations at different numbers of particles, N, and cell dimensions $L = [d, w, h]$, where the parallel sidewalls are separated by the distance d, $n = N/(dwh)$. Simulations are at truncation $N_k = 15$ except the $16d = w = h$ simulation, at $N_k = 29$, to mimic similar spatial resolution of the point-force advection fields. (*a*) Data in units; (*b*) scaled assuming Caflisch & Luke (1985) scaling with d as the relevant length scale.

velocity scale changes like $V_0\sqrt{\phi d/a}$, as the independent Poisson distribution predicts. Necessarily, the effective diffusivity of the particles then scales as the product of the correlation length, ℓ (with $\ell \sim d$ in vertically homogeneous sedimentation), and the characteristic velocity scale, ΔV.

B.3. *Fluctuations of fluctuations*

We define the variance of the velocity variances, $\sigma^2(\Delta V^2) = \langle (\Delta \langle \Delta V^2 \rangle_N)^2 \rangle_t$, with the velocity variances determined by averaging over all particles (depth averaging) at each time step, taking the variance of this random variable as it varies in time. The determination of $\Delta V^2(t)$ at each time is a sample mean for the true $\langle \Delta V^2 \rangle$, averaging over the N individual particle fluctuations. The variance of this sample mean, for independent particle *responses* (as opposed to independent source positions), would be

$$\sigma^2\left(\Delta V_\alpha^2\right)_{\text{ind.response}} = \frac{1}{N^2}\sum_i \left[\Delta\left(V_\alpha^i - \langle V_\alpha\rangle\right)^2\right]^2 = \frac{1}{N}\left[\left\langle \Delta V_\alpha^4\right\rangle - \left\langle \Delta V_\alpha^2\right\rangle^2\right]. \tag{B 1}$$

The calculation of the velocity variance reduces to an integral over the square of the flow generated by a single particle, $[u_\alpha(\boldsymbol{r}, \boldsymbol{r}_0)]^2$, as in (2.1), with the cross-terms in the square of the ith particle velocity, $V^{(i)}$, multiplying flows from two different source particles averaging to zero according to the no-net-flow $\langle u_\alpha\rangle = 0$ condition and the independent positions assumption. Likewise, the third moments of the velocity distributions reduce to an integral over $[u_\alpha(\boldsymbol{r}, \boldsymbol{r}_0)]^3$, cross-terms multiplying contributions from two and from three source particles similarly reducing to zero for independent particle distributions. Horizontal third moments are then predicted to be zero by symmetry, while vertical skewnesses, $\langle \Delta V_z^3\rangle / \langle \Delta V_z^2\rangle^{3/2}$, are expected to be negative (for downward velocities being negative, that is, skewed towards falling faster), because of the vertical asymmetry of the generated flows, and are observed to be $O(-0.1)$ in simulations. Meanwhile, the fourth power of the sum of the individual contributions to the velocity of the ith particle includes squared cross-terms that remain under averaging, yielding

$$\left\langle \Delta V_\alpha^4\right\rangle(x) = 3\left\langle \Delta V_\alpha^2\right\rangle^2(x) + n\int_{r>a} \mathrm{d}\boldsymbol{r}_0\, [u_\alpha(\boldsymbol{r}, \boldsymbol{r}_0)]^4, \tag{B 2}$$

the latter integral, scaling like ϕV_0^4, giving a negligible contribution in large cells.

The predicted Pearson kurtosis at a given interwall position is then 3, with the depth-averaged kurtosis $\kappa = \langle \Delta V^4\rangle / \langle \Delta V^2\rangle^2$ when averaging over all particles predictably deviating above 3 according to the ratio of $\langle C_\alpha(x)^4\rangle$ to $\langle C_\alpha(x)^2\rangle$ (2.3).† We note that the independent-Poisson assumption predicts weakly non-Gaussian velocity distributions, with non-zero skewness and non-Gaussian kurtosis for depth-averaged statistics in the presence of sidewalls (cf. theoretical calculations by Tory, Bargiel & Kamel 1993, quasi-two-dimensional experimental observations of Rouyer, Martin & Salin 1999, and numerical simulations by Miguel & Pastor-Satorras 2001).

The depth-averaged Pearson kurtosis, relative to the depth-averaged Poisson prediction, is plotted in figure 13(*a*) for a series of simulations at different cell aspect ratios; the Poisson prediction κ_{Poisson} is found to be accurate to within a couple of percent in most cases there. If the particle *responses* were independent, $\sigma^2(\Delta V_\alpha^2)_{\text{ind.response}} \approx 2\langle \Delta V_\alpha^2\rangle^2$; but while independent particle source positions is a good assumption for vertically homogeneous sedimentation, the resulting particle velocities appear as swirl structures (e.g. as in figure 1 and Segrè *et al.* 1997), the particle responses being clearly correlated over the length scale of a swirl. We thus conjecture that $\sigma^2(\Delta V^2) \sim \langle \Delta V^2\rangle^2 / N_{\text{swirls}}$ where N_{swirls} is the number of swirls in the cell. With the small dimension d setting the size of the swirls in a $d \times w \times h$ cell with $d \ll w, h$, we then expect

$$\sigma^2\left(\Delta V_\alpha^2\right) \sim \frac{\left\langle \Delta V_\alpha^2\right\rangle^2}{wh/d^2}. \tag{B 3}$$

---

† Again, we remark that comparison with numerical simulations requires truncating the velocity fields at the same number of Fourier modes as used in the simulation, which is an artifact of the numerical simulations, having no bearing on the infinite truncation $N_k \to \infty$ limit.

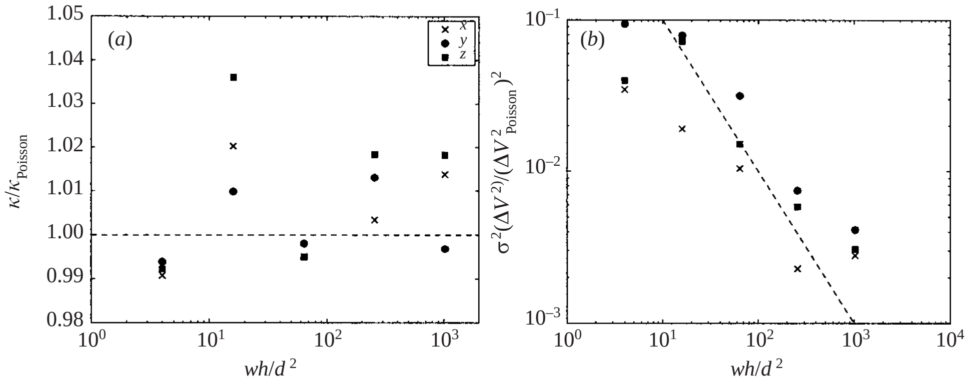

FIGURE 13. Higher-order statistics for each velocity component observed in a series of very long-running simulations at various aspect ratios ($d \times w \times h$ cells): (a) the depth-averaged Pearson kurtosis $\kappa = \langle \Delta V^4 \rangle / \langle \Delta V^2 \rangle^2$ relative to its Poisson prediction, $\kappa_{Poisson} = \Delta V^4_{Poisson}/(\Delta V^2_{Poisson})^2$ (B 2), (2.3); and (b) the variance of the velocity variance, $\sigma^2(\Delta V^2)$, relative to $(\Delta V^2_{Poisson})^2$, compared with a $(wh/d^2)^{-1}$ dashed line (B 3).

Long-running simulations confirm that $\sigma^2(\Delta V^2)/\langle \Delta V^2 \rangle^2$ is independent of the number of particles, N, and only weakly dependent on the truncation for sufficiently large values of N_k (roughly, enough to adequately resolve the spatial dependence of flow fields significantly below the swirl size). Results for the variance of the velocity variance obtained in a series of simulations at different cell aspect ratios are plotted in figure 13(b), in reasonable agreement at large aspect ratios with the $(wh/d^2)^{-1}$ scaling proposed in (B 3). Significantly greater quantities of data would need to be generated to more closely check this dependence.

REFERENCES

BATCHELOR, G. K. 1972 Sedimentation in a dilute suspension of spheres. *J. Fluid Mech.* **52**, 245–268.

BERGOUGNOUX, L., GHICINI, S., GUAZZELLI, E. & HINCH, J. 2003 Spreading fronts and fluctuations in sedimentation. *Phys. Fluids* **15**, 1875–1887.

BLAKE, J. R. 1971 A note on the image system for a Stokeslet in a no-slip boundary. *Proc. Camb. Phil. Soc.* **70**, 303–310.

BOYCOTT, A. E. 1920 Sedimentation of blood corpuscles. *Nature* **104**, 532.

BRADY, J. F. & BOSSIS, G. 1988 Stokesian dynamics. *Annu. Rev. Fluid Mech.* **20**, 111–157.

BRENNER, M. P. 1999 Screening mechanisms in sedimentation. *Phys. Fluids* **11**, 754–772.

CAFLISCH, R. E. & LUKE, J. H. C. 1985 Variance in the sedimentation speed of a suspension. *Phys. Fluids* **28**, 759–760.

COWAN, M. L., PAGE, J. H. & WEITZ, D. A. 2000 Velocity fluctuations in fluidized suspensions probed by ultrasonic correlation spectroscopy. *Phys. Rev. Lett.* **85**, 453–456.

DAVIS, R. H. & ACRIVOS, A. 1985 Sedimentation of noncolloidal particles at low Reynolds numbers. *Annu. Rev. Fluid Mech.* **17**, 91–118.

GUAZZELLI, E. 2001 Evolution of particle-velocity correlations in sedimentation. *Phys. Fluids* **13**, 1537–1540.

HAM, J. M. & HOMSY, G. M. 1988 Hindered settling and hydrodynamic dispersion in quiescent sedimenting suspensions. *Intl J. Multiphase Flow* **14**, 533–546.

HINCH, E. J. 1988 Sedimentation of small particles. In *Disorder and Mixing* (ed. E. Guyon, J.-P. Nadal & Y. Pomeau), chap. IX, pp. 153–161. Kluwer.

Kermack, W. O., M'Kendrick, A. G. & Ponder, E. 1929 The stability of suspensions. III. The velocities of sedimentation and of cataphoresis of suspensions in a viscous fluid. *Proc. R. Soc. Edinburgh* **49**, 170–197.

Koch, D. L. 1994 Hydrodynamic diffusion in a suspension of sedimenting point particles with periodic boundary conditions. *Phys. Fluids* **6**, 2894–2900.

Koch, D. L. & Shaqfeh, E. S. G. 1991 Screening in sedimenting suspensions. *J. Fluid Mech.* **224**, 275–303.

Kuusela, E. & Ala-Nissila, T. 2001 Velocity correlations and diffusion during sedimentation. *Phys. Rev.* E **63**, 061505.

Ladd, A. J. C. 1990 Hydrodynamic transport coefficients of random dispersions of hard spheres. *J. Chem. Phys.* **93**, 3484–3494.

Ladd, A. J. C. 1993 Dynamic simulations of sedimenting spheres. *Phys. Fluids* A **5**, 299–310.

Ladd, A. J. C. 1994 Numerical simulations of particulate suspensions via a discretized Boltzmann equation. Part 1 Theoretical foundation. *J. Fluid Mech.* **271**, 285–309.

Ladd, A. J. C. 1996 Hydrodynamic screening in sedimenting suspensions of non-Brownian spheres. *Phys. Rev. Lett.* **76**, 1392–1395.

Ladd, A. J. C. 1997 Sedimentation of homogeneous suspensions of non-Brownian spheres. *Phys. Fluids* **9**, 491–499.

Ladd, A. J. C. 2002 Effects of container walls on the velocity fluctuations of sedimenting spheres. *Phys. Rev. Lett.* **88**, 048301.

Lei, X., Ackerson, B. J. & Tong, P. 2001 Settling statistics of hard sphere particles. *Phys. Rev. Lett.* **86**, 3300–3303.

Levine, A., Ramaswamy, S., Frey, E. & Bruinsma, R. 1998 Screened and unscreened phases in sedimenting suspensions. *Phys. Rev. Lett.* **81**, 5944–5947.

Liron, N. & Mochon, S. 1976 Stokes flow for a Stokeslet between two parallel flat plates. *J. Engng Maths* **10**, 287–303.

Luke, J. H. C. 2000 Decay of velocity fluctuations in a stably stratified suspension. *Phys. Fluids* **12**, 1619–1621.

Martin, J., Rakotomalala, N. & Salin, D. 1994 Hydrodynamic dispersion broadening of a sedimentation front. *Phys. Fluids* **6**, 3215–3217.

Mazur, P. & van Saarloos, W. 1982 Many-sphere hydrodynamic interactions and mobilities in a suspension. *Physica* A **115**, 21–57.

Miguel, M. C. & Pastor-Satorras, R. 2001 Velocity fluctuations and hydrodynamic diffusion in sedimentation. *Europhys. Lett.* **54**, 45–50.

Mucha, P. J. & Brenner, M. P. 2003 Diffusivities and front propagation in sedimentation. *Phys. Fluids* **15**, 1305–1313.

Nicolai, H. & Guazzelli, E. 1995 Effect of the vessel size on the hydrodynamic diffusion of sedimenting spheres. *Phys. Fluids* **7**, 3–5.

Nicolai, H., Herzhaft, B., Hinch, E. J., Oger, L. & Guazzelli, E. 1995 Particle velocity fluctuations and hydrodynamic self-diffusion of sedimenting non-brownian spheres. *Phys. Fluids* **7**, 12–23.

Pulvirenti, M. 1996 Kinetic limits for stochastic particle systems. In *Probabilistic Models for Nonlinear Partial Differential Equations* (ed. D. Talay & L. Tubaro). Lecture Notes in Mathematics, vol. 1627. Springer.

Ramaswamy, S. 2001 Issues in the statistical mechanics of steady sedimentation. *Adv. Phys.* **50**, 297–341.

Rouyer, F., Martin, J. & Salin, D. 1999 Non-gaussian dynamics in quasi-2d noncolloidal suspensions. *Phys. Rev. Lett.* **83**, 1058–1061.

Sangani, A. S. & Mo, G. 1996 An O(N) algorithm for Stokes and Laplace interactions of particles. *Phys. Fluids* **8**, 1990–2010.

Schwarzer, S., Hofler, K., Manwart, C., Wachmann, B. & Herrman, H. 1999 Non-Brownian suspensions: simulation and linear response. *Physica* A **266**, 249–254.

Segrè, P. N., Herbolzheimer, E. & Chaikin, P. M. 1997 Long-range correlations in sedimentation. *Phys. Rev. Lett.* **79**, 2574–2577.

Segrè, P. N., Liu, F., Umbanhowar, P. & Weitz, D. A. 2001 An effective gravitational temperature for sedimentation. *Nature* **409**, 594–597.

Tee, S.-Y., Mucha, P. J., Cipelletti, L., Manley, S., Brenner, M. P., Segrè, P. N. & Weitz, D. A. 2002 Nonuniversal velocity fluctuations of sedimenting particles. *Phys. Rev. Lett.* **89**, 054501.

Tory, E. M., Bargiel, M. & Kamel, M. T. 1993 The distribution of velocities of a concentric sphere in a dilute dispersion of spheres sedimenting in a spherical container. *Powder Technol.* **74**, 159–169.

Xue, J. Z., Herbolzheimer, E., Rutgers, M. A., Russel, W. B. & Chaikin, P. M. 1992 Diffusion, dispersion, and settling of hard-spheres. *Phys. Rev. Lett.* **69**, 1715–1718.